

# Simulations of Concrete Response to Impact Loading Using Two Regularized Models

Adam WOSATKO\*, Andrzej WINNICKI, Jerzy PAMIN

*Cracow University of Technology  
Faculty of Civil Engineering*

Warszawska 24, 31-155 Cracow, Poland

e-mail: andrzej@hypatia.L5.pk.edu.pl, jpamin@L5.pk.edu.pl

\*Corresponding Author e-mail: awosatko@L5.pk.edu.pl

This paper focuses on a comparison of two regularized continuum models for concrete in the simulations of selected benchmarks of response to impact loading. Their overview is performed in the context of application in dynamics. The first one is the Hoffman viscoplastic consistency model, where the strain rate activates regularization. The second model is derived from the scalar damage theory enhanced by an averaging equation incorporating the Laplacian of an averaged strain measure. Both models are implemented in the FEAP package. The results of some standard wave propagation tests are discussed, considering discretization sensitivity and predicted failure modes. Three examples are presented: the direct tension of a plain and reinforced concrete bar, the split test of a cylinder, and the four-point bending of a reinforced concrete beam. The ability of both models to simulate impact loading is assessed.

**Keywords:** dynamics, viscoplasticity, damage, concrete, regularization, finite element method.

## 1. INTRODUCTION

The initial boundary value problem (IBVP), where an impact loading has been introduced, is solved using numerical analysis to examine wave propagation effects in concrete structures. For dynamics, the following equations of motion are considered:

$$\mathbf{L}^T \boldsymbol{\sigma} + \mathbf{b} = \rho \ddot{\mathbf{u}}, \quad (1)$$

where  $\mathbf{L}$  is a matrix of differential operators,  $\boldsymbol{\sigma}$  is the stress tensor in a vector form,  $\mathbf{b}$  is the body force vector, and  $\rho \ddot{\mathbf{u}}$  represents inertia forces with density  $\rho$  and acceleration vector  $\ddot{\mathbf{u}}$ . Small strains and no damping are assumed. The Voigt

(matrix-vector) notation is applied in the paper. The simplest test is an extension of a bar in one dimension. After imposing an impulse, for elastic materials, an incoming wave reflects from a boundary and runs further in the opposite direction. The distribution of the axial strain against time and length of the bar is shown in Fig. 1a. Such a phenomenon of wave propagation and reflection is typical for the elasticity theory.

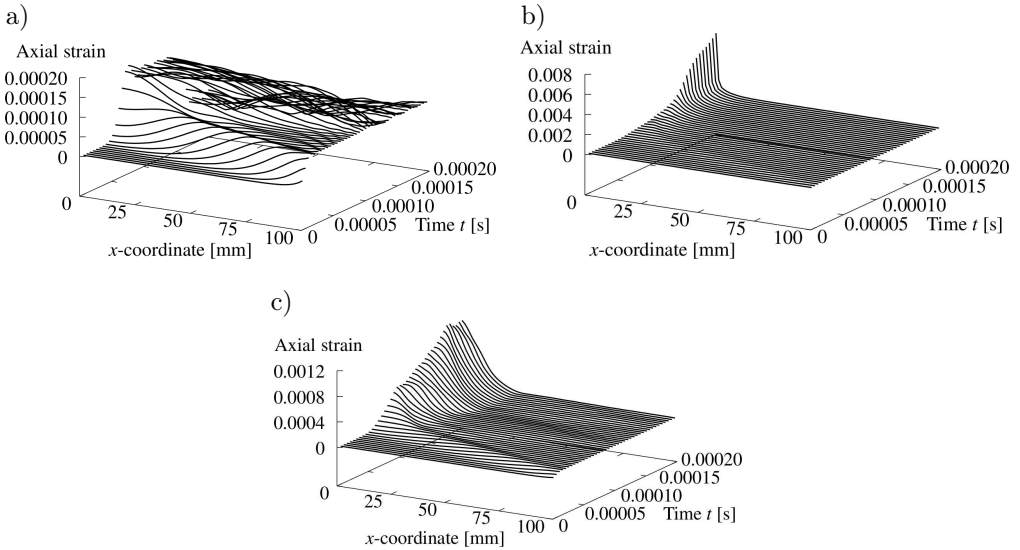


FIG. 1. Bar under one-dimensional tension – lengthwise change of axial strain in time: a) elasticity, b) local model, c) regularized model.

Concrete is initially modelled as an elastic material, but when the stress is large enough, it behaves as a quasi-brittle material. Generally, strain localization and cracking occur in concrete, hence softening of the material is observed for advanced stress states. The presence of strain localization in concrete is shown in various experiments, see, e.g., [24, 28, 31, 36, 61]. The analytical solution of a strain-softening bar in dynamics explains the mechanism of propagating and stopping waves, see [3, 54]. When the stress exceeds the elastic limit after the wave front reaches a boundary and reflects, softening is observed, imaginary wave speeds are obtained and, hence, waves do not propagate, i.e., a standing wave occurs. In a local continuum, a displacement discontinuity can be a result of the standing wave and then the strain at the place of localization can be represented by a Dirac delta function. Hence, in the local approach the zone of intense deformation is limited to a discrete line (curve) or plane (surface). Figure 1b depicts the surface plot of the axial strain for a local model, i.e., without any regularization.

A proper description of material softening cannot be included directly into the stress-strain relation for local continuum models, because the hyperbolic character of the IBVP for dynamics changes into elliptic. Such a transition means that the IBVP becomes ill-posed. Mathematically, the ill-posedness of the IBVP is the cause of an infinite number of solutions. Hence, the loss of hyperbolicity provokes spurious mesh sensitivity in the finite element approximation. It coincides with the onset of strain localization. The formation of a crack zone is limited to the possibly narrowest band admitted by a discretization, e.g., one row of finite elements. Remaining within the continuum description, this issue can be overcome using different regularization techniques with the so-called localization limiters. In [6], three types of limiters are distinguished: rate, differential and integral. It can be observed in Fig. 1c that the propagating wave changes into a standing wave, but the influence of regularization (in this particular case – gradient damage) is visible as a smoothed function of the axial strain governed by the limiter and not the discretization. It is also noticed that the elastic part of the propagating energy results in small running humps.

The model can be regularized by an additional viscous term (the rate-type limiter) included in the constitutive relation. The viscoplasticity theory has been known for many years, see, for instance, [43], and it is still effectively exploited as in, e.g., [23, 40, 52]. It is confirmed in [54] that the viscous regularization is more powerful in dynamics than statics. The other option is the application of a higher-order model for the damage theory via a so-called gradient enhancement [41] (the differential limiter). The gradient damage model can be employed not only in the analysis of concrete but, e.g., for biomaterials [63] or even more generally, for other materials that undergo large deformations [33, 66]. Nonlocal integral-type models are not considered in this paper, but numerous works where they are applied to concrete can be found, e.g., [4, 5, 8, 25, 34]. It is stressed that the mezo-scale modelling, see, e.g., [53], can prompt the macromodel enhancements and provide an internal length scale estimation. Moreover, multiscale analyses of concrete have also been performed [22, 30].

The finite element method (FEM) has been used to investigate the impact loading and dynamic failure of concrete in different tests, for example, panel in compact tension [37], RC beams and deep beams [57], RC slabs [11, 60], and tunnel cylindrical shells [12]. In this paper, selected FEM simulations of dynamic tests under impact loading for concrete specimens made by means of two regularized continuum models are discussed. In Sec. 2, both models are briefly characterized. The first one is the Hoffman viscoplastic consistency model [64, 69] (called HVP in the paper), the second is the gradient damage model [13, 14, 41] (called GDA in the paper). Section 3 consists of a description of the results for the benchmarks: direct tension of a bar, cylinder splitting and four-point bending of a beam. Two-dimensional configurations are

considered. Sensitivities to mesh density and loading rate are examined. Finally, in Sec. 4 conclusions are summarized.

## 2. OVERVIEW OF MATERIAL MODELS FOR IMPACT ANALYSIS

### 2.1. Hoffman viscoplastic consistency model

The first constitutive model based on the plasticity theory is regularized via a viscous term. Usually the viscoplastic models take over the approaches invented by Perzyna [43] or Duvaut-Lions [17], in which the viscoplastic strains are determined using the viscosity parameter (relaxation time) in the explicit way. The model described below is called consistency viscoplasticity model and follows the idea proposed in [64] for metals and then developed, e.g., in [10, 27].

It is admitted that the yield function can expand or shrink depending on the actual viscoplastic strain rate. The stress state is forced to remain on the yield surface and the consistency condition is invoked. There is no additional equation defining a viscoplastic multiplier. Instead, in the consistency condition two separate hardening material moduli appear: a classical plastic one  $h$  and a viscoplastic one  $s$ . Abbreviation HVP is introduced to refer to the employed Hoffman viscoplastic consistency model. The Burzyński-Hoffman yield surface in its isotropic form is selected since it has been successfully applied in the analysis of concrete structures [7]:

$$F^{\text{VP}} = q^2 + 3p(f_c - f_t) - f_c f_t = 0, \quad (2)$$

where  $p = \text{tr}(\boldsymbol{\sigma})/3$  is the hydrostatic pressure and  $q = \sqrt{3 \text{tr}(\boldsymbol{s}^2)}/2$  is the Huber-Mises deviatoric measure of the stress tensor  $\boldsymbol{\sigma}$  (written in a vector form). The deviatoric stress tensor is calculated as  $\boldsymbol{s} = \boldsymbol{\sigma} - p\boldsymbol{I}$ , where  $\boldsymbol{I}$  is the identity matrix. Two internal variables  $\kappa_c$  and  $\kappa_t$  are postulated. They are both functions of the equivalent viscoplastic strain and separately specify the material hardening/softening in compression and tension, respectively. In addition, two more internal variables  $\eta_c$  and  $\eta_t$  determine the increase/decrease of compressive and tensile strengths due to the current equivalent viscoplastic strain rate. The respective rate-dependent strengths become functions:

$$f_c = f_c(\kappa_c, \eta_c) \quad \text{and} \quad f_t = f_t(\kappa_t, \eta_t). \quad (3)$$

The dependence of  $f_i$  on  $\kappa_i$  and  $\eta_i$  is formulated in a general way as  $f_i = f_i' H_i(\kappa_i) S_i(\eta_i)$  for compression ( $i = c$ ) and tension ( $i = t$ ), respectively, where  $f_i'$  is the initial compressive/tensile strength. The functions  $H_i$  and  $S_i$  can be defined in different manners, e.g., as piecewise linear, see Figs 3, 8c, 23c and 23d in the next sections. The rates of the internal variables depend on the current stress and the rates of internal variables  $\kappa$  and  $\eta$ :

$$\dot{\kappa}_i = g_i(\boldsymbol{\sigma})\dot{\kappa} \quad \text{and} \quad \dot{\eta}_i = g_i(\boldsymbol{\sigma})\dot{\eta}, \quad (4)$$

where subscript  $i$  still stands for  $c$  or  $t$ . In the above, relations  $g_i$  are scalar functions accounting for independent processes of damage in compression and tension. The functions  $g_i$  are chosen in accordance with experiments, taking into account the influence of the damage process in compression on the concrete strength in tension and, vice versa, the influence of the damage process in tension on the concrete strength in compression. In [68] two variants are considered. In the first option, damage is assumed as an isotropic phenomenon, hence  $g_c = g_t = 1$  and  $\kappa_c = \kappa_t$ . In the second approach, the response is different in tension and compression, hence it is assumed that  $g_c + g_t = 1$ . In extreme cases for dominant compressive stress  $g_c = 1$ ,  $g_t = 0$  and for dominant tensile stress  $g_c = 0$ ,  $g_t = 1$ .

In turn,  $\dot{\kappa}$  is determined as an equivalent viscoplastic strain rate assuming work hardening, while  $\dot{\eta}$  depends on the time derivative of the viscoplastic strain rate:

$$\dot{\kappa} = \boldsymbol{\sigma}^T \dot{\boldsymbol{\epsilon}}^{\text{vp}} / q \quad \text{and} \quad \dot{\eta} = \boldsymbol{\sigma}^T \ddot{\boldsymbol{\epsilon}}^{\text{vp}} / q. \quad (5)$$

In the course of loading the yield surface can change its shape due to the separate hardening/softening processes of the compressive and tensile strength, but the surface remains convex at all times. It is not only a function of the internal parameter  $\kappa$ , but also of the additional one  $\eta$ . Since the total value of  $\eta$  depends on the first time derivatives of viscoplastic strains, the yield surface is rate-dependent, i.e., it expands for higher and shrinks for lower viscoplastic strain rates. As a result, this model can correctly predict basic viscoplastic phenomena like creep and relaxation.

In the HVP model, the strain rate is decomposed into its elastic and viscoplastic parts, and the generalized Hooke law is valid for the elastic part:

$$\dot{\boldsymbol{\epsilon}} = \dot{\boldsymbol{\epsilon}}^e + \dot{\boldsymbol{\epsilon}}^{\text{vp}}, \quad \dot{\boldsymbol{\sigma}} = \mathbf{E} \dot{\boldsymbol{\epsilon}}^e, \quad (6)$$

where  $\mathbf{E}$  is the elastic stiffness operator. The viscoplastic flow rule is defined similarly to the classical associated plasticity:

$$\dot{\boldsymbol{\epsilon}}^{\text{vp}} = \dot{\lambda} \mathbf{n}, \quad \mathbf{n} = \frac{\partial F^{\text{vp}}}{\partial \boldsymbol{\sigma}}. \quad (7)$$

The consistency equation is employed in order to establish the viscoplastic multiplier  $\dot{\lambda}$ :

$$\mathbf{n}^T \dot{\boldsymbol{\sigma}} - h \dot{\lambda} - s \ddot{\lambda} = 0. \quad (8)$$

Due to the last term the consistency equation is no longer an algebraic equation for the viscoplastic multiplier, but a differential equation of the first order,

to be solved for an appropriate initial condition. The generalized plastic and viscoplastic moduli are computed as:

$$h = a_c S_c h_c + a_t S_t h_t \quad \text{and} \quad s = a_c s_c H_c + a_t s_t H_t, \quad (9)$$

where

$$h_i = \frac{dH_i}{d\kappa_i} \quad \text{and} \quad s_i = \frac{dS_i}{d\eta_i}, \quad (10)$$

and the other coefficients are as follows:

$$a_c = f'_c (f_t - \text{tr } \boldsymbol{\sigma}) g_c g \quad \text{and} \quad a_t = f'_t (f_c + \text{tr } \boldsymbol{\sigma}) g_t g. \quad (11)$$

One more definition is needed:

$$g = \boldsymbol{\sigma}^T \mathbf{n} / q. \quad (12)$$

When functions  $S_c$  and  $S_t$  are constant, their derivatives vanish and Eq. (8) reduces to the form known from the classical rate independent plasticity. It is widely discussed in [68] how the material model parameters can be linked with the fracture energies  $G_{ft}$  and  $G_{fc}$ , which are the actual material properties [20, 61, 62], via the width of the localization zone. If  $S_t = S_c \equiv 1$  then the localization limiter is missing in the HVP model and the width of the crack zone usually coincides with one row of finite elements. The viscous term is turned off and the lack of regularization can be observed. On the other hand, when viscous effects are active, the width of the localization zone is determined and the HVP model becomes regularized.

It should finally be mentioned that the implementation of the HVP model in dynamics is analogous to the classical rate-independent plasticity. The weak form of the equations of motion (1) is discretized in a standard way. The initial boundary value problem (IBVP) is linearized and an implicit time-integration using the standard Newmark algorithm is applied. Displacement field  $\mathbf{u}$  is approximated via the proper shape functions  $\mathbf{N}$  and the nodal vector of displacement degrees of freedom  $\mathbf{a}$ :

$$\mathbf{u} = \mathbf{N} \mathbf{a}. \quad (13)$$

The following matrix equation is solved in each computed time step:

$$\mathbf{M}_{aa} \ddot{\mathbf{a}}^{t+\Delta t} + \mathbf{K}_{aa} \Delta \mathbf{a} = \mathbf{f}_{\text{ext}}^{t+\Delta t} - \mathbf{f}_{\text{int}}^t. \quad (14)$$

Inertia effects are present, and consequently, the consistent mass matrix is included:

$$\mathbf{M}_{aa} = \int_{\mathcal{B}} \mathbf{N}^T \rho \mathbf{N} dV. \quad (15)$$

Appropriate definitions of tangent stiffness operator  $\mathbf{K}_{aa}$ , external forces  $\mathbf{f}_{\text{ext}}$  and internal forces  $\mathbf{f}_{\text{int}}$  are provided in Appendix. The aforementioned model is programmed as a usermat subroutine in the FEAP package [58].

## 2.2. Gradient-enhanced damage model

The second model used in this paper, based on continuum damage mechanics, describes elastic stiffness degradation in quasi-brittle materials. This model is additionally equipped with a so-called implicit gradient enhancement to ensure mesh-objective results. In the simplest version, one damage measure  $\omega$  [29], which grows from 0 (no damage) to 1 (complete loss of stiffness), is a function of damage history parameter  $\kappa^d$  and depends on the deformation of a body. The concept of strain equivalence in the real and effective (fictitious) configuration is assumed, see, e.g., [48]. The effective stress tensor  $\hat{\boldsymbol{\sigma}}$  (in a vector form) acts on the undamaged material skeleton while the actual stress  $\boldsymbol{\sigma}$  satisfies the motion Eq. (1). The stress tensors are related by parameter  $\omega$ :

$$\boldsymbol{\sigma} = (1 - \omega) \hat{\boldsymbol{\sigma}}, \quad \hat{\boldsymbol{\sigma}} = \mathbf{E} \boldsymbol{\epsilon}^e. \quad (16)$$

The elastic strain tensor  $\boldsymbol{\epsilon}^e$  is equal to the strain tensor  $\boldsymbol{\epsilon}$  when the standard elasto-damage model is considered (this paper is limited to this case). However the model can easily be coupled with a plastic behaviour of the undamaged material “skeleton” and then  $\boldsymbol{\epsilon}^e = \boldsymbol{\epsilon} - \boldsymbol{\epsilon}^p$  according to the standard additive decomposition, where  $\boldsymbol{\epsilon}^p$  is the plastic strain tensor. Then for unloading, irreversible strains can be observed in concrete. In that case, the motivation for coupling the damage model with plasticity is substantial, see, e.g., [1, 14]. Moreover, the constitutive relations can incorporate a projection operator as in, e.g., [67, 70] to reproduce the crack closing effect. These aspects are skipped in this paper because attention is focused only on the dynamic analysis.

The strain equivalence is related with a damage loading function  $F^d$ , determined in the strain space:

$$F^d(\boldsymbol{\epsilon}, \kappa^d) = \tilde{\epsilon}(\boldsymbol{\epsilon}) - \kappa^d = 0, \quad (17)$$

where  $\tilde{\epsilon}$  defines an equivalent strain measure. During the damage evolution, the parameter  $\kappa^d$  corresponds to the largest value of  $\tilde{\epsilon}$  reached in the loading history and the Kuhn-Tucker conditions are in force. The equivalent strain measure  $\tilde{\epsilon}$  can be defined in many ways. The modified von Mises definition [15] is employed in this paper:

$$\tilde{\epsilon} = \frac{(k-1)I_1^\epsilon}{2k(1-2\nu)} + \frac{1}{2k} \sqrt{\left(\frac{(k-1)I_1^\epsilon}{1-2\nu}\right)^2 + \frac{12kJ_2^\epsilon}{(1+\nu)^2}}, \quad (18)$$

where  $k = f'_c/f'_t$  is the ratio of uniaxial compressive and tensile strengths,  $\nu$  is Poisson's ratio, and  $I_1^\epsilon$  and  $J_2^\epsilon$  are the strain invariants. The above definition introduces the sensitivity of the model to the sign of strains and allows for damage not only under tension but also under (biaxial) compression. However, the interaction of tensile and compressive effects in concrete is not represented as accurately as in the HVP model. The damage growth can be determined using an exponential relation [35]:

$$\omega(\kappa^d) = 1 - \frac{\kappa_o}{\kappa^d} \left( 1 - \alpha + \alpha e^{-\eta(\kappa^d - \kappa_o)} \right), \quad (19)$$

where  $\kappa_o$  is the damage threshold, and the respective parameters  $\eta$  and  $\alpha$  are responsible for material ductility and residual stress. The former parameter is thus connected with concrete fracture energy  $G_{ft}$ . The latter precludes the complete loss of material stiffness and makes the numerical response more stable. According to the experiment [28], uniaxial softening for tension is an exponential function, so when  $\kappa^d$  exceeds the value of damage threshold  $\kappa_o$ , then damage  $\omega$  asymptotically grows to 1.

In this model, the regularization is introduced including the second gradient of the averaged (nonlocal) strain  $\bar{\epsilon}$  in the implicit form of the additional diffusion-type equation according to [41]:

$$\bar{\epsilon} - c \nabla^2 \bar{\epsilon} = \tilde{\epsilon}, \quad (20)$$

and homogeneous natural boundary conditions  $(\nabla \bar{\epsilon})^T \boldsymbol{\nu} = 0$ , where  $\boldsymbol{\nu}$  is the outward normal to the domain boundary. The parameter  $c > 0$ , assumed in the computations to be constant, has a unit of length squared and corresponds to an internal length scale  $l$  by means of the relation  $c = \frac{1}{2} l^2$  [2]. The damage evolution in the gradient-enhanced model is governed by the following damage activation function:

$$F^d(\boldsymbol{\epsilon}, \kappa^d) = \bar{\epsilon}(\tilde{\epsilon}(\boldsymbol{\epsilon})) - \kappa^d = 0. \quad (21)$$

Although some reservations have been raised with respect to this model, cf. [21, 42, 51, 65], it is applied here for dynamics in its original form. Further, abbreviation GDA will be used for the implicit gradient damage model. Some developments of the model with reference to dynamics are explored, e.g., in [26, 32, 65].

The equations of motion (1) have to be investigated to analyze the wave propagation in the IBVP. Collateral presence of Eq. (20) leads to preservation of the well-posedness of the IBVP. Hence, not the element size governs the solution but the employed internal length scale. After introducing space and time

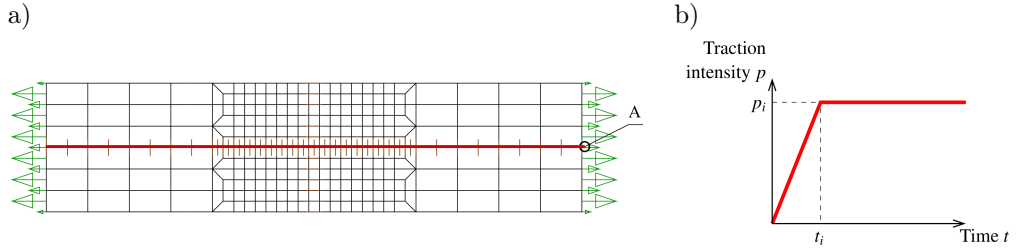


FIG. 2. Dynamic direct tension test – configuration and loading history:  
 a) configuration and applied mesh, b) loading history.

discretization into the two-field gradient damage formulation, the model can be described by the system of equations analogous to gradient plasticity in [54]:

$$\begin{bmatrix} \mathbf{M}_{aa} & 0 \\ 0 & 0 \end{bmatrix} \begin{bmatrix} \ddot{\mathbf{a}}^{t+\Delta t} \\ \ddot{\mathbf{e}}^{t+\Delta t} \end{bmatrix} + \begin{bmatrix} \mathbf{K}_{aa} & \mathbf{K}_{ae} \\ \mathbf{K}_{ea} & \mathbf{K}_{ee} \end{bmatrix} \begin{bmatrix} \Delta \mathbf{a} \\ \Delta \mathbf{e} \end{bmatrix} = \begin{bmatrix} \mathbf{f}_{\text{ext}}^{t+\Delta t} - \mathbf{f}_{\text{int}}^t \\ \mathbf{f}_{\epsilon}^t - \mathbf{f}_e^t \end{bmatrix}. \quad (22)$$

Displacement and averaged strain measure fields are interpolated independently using nodal vectors  $\mathbf{a}$  and  $\mathbf{e}$ , respectively. The mass matrix influences only the discrete motion equations, while the non-symmetric tangent operator in the second component couples both approximated fields. The definitions of other submatrices and subvectors are given in Appendix. The nonlinear IBVP for the GDA model is solved in each computed time step by means of implicit time-integration based on the standard Newmark algorithm. Moreover, as for the HVP model, within the time steps, the Newton-Raphson method is applied to retrieve internal equilibrium. The in-house code for the user-element is implemented in the FEAP program [58].

### 3. NUMERICAL EXAMPLES OF IMPACT ANALYSIS

#### 3.1. Direct tension test

The first test is an analysis of tensile wave propagation of a 2D bar under a dynamic load for two cases: plain and reinforced concrete (RC). The results are confronted for the two regularized models discussed in the previous section: Hoffman viscoplasticity (HVP) and gradient damage (GDA). It should be mentioned that the results of this test for the GDA model were also presented in [71] and here they are only briefly recapitulated for the completeness of the paper. This should help in a better understanding of the presence of the regularizing contribution in both models in the context of impact loading. A similar comparison for gradient-enhanced plasticity and damage models for plain concrete is presented in [38].

The configuration of the test is depicted in Fig. 2a, where the bar supported along both symmetry axes is considered. A time-dependent normal traction on both (left and right) sides according to the function presented in Fig. 2b is adopted, where the traction intensity  $p_i = 2.4$  MPa becomes constant for time instant  $t_i = 3 \times 10^{-5}$  s = 30  $\mu$ s. The time step in the computations is 2  $\mu$ s. The length of the bar is  $L = 250$  mm, and the height is  $H = 60$  mm. Plane stress conditions are analyzed and the thickness  $T = 50$  mm is assumed. The FE mesh is also illustrated in Fig. 2a. Eight-noded elements are employed for concrete. The suitable combination of quadratic interpolation of the displacements  $\mathbf{a}$  and linear of the averaged strain  $\mathbf{e}$  is introduced for the GDA model, cf. discussion in [49]. It is visible that the zone in the centre is refined because localization is expected there. When the RC bar is computed, the reinforcement is located along the horizontal axis and elastic truss elements are applied to discretize it.

The material data of concrete are as follows: Young's modulus  $E = 18000$  MPa, Poisson's ratio  $\nu = 0.0$  and density  $\rho = 2320$  kg/m<sup>3</sup>. Initial tensile strength  $f'_t = 3.40$  MPa and initial compressive strength  $f'_c = 34$  MPa are assumed. If the HVP model is used then material functions have to be defined. Function  $H_c$  for compression shown in Fig. 3a depends on the equivalent viscoplastic strain  $\kappa_c$ .

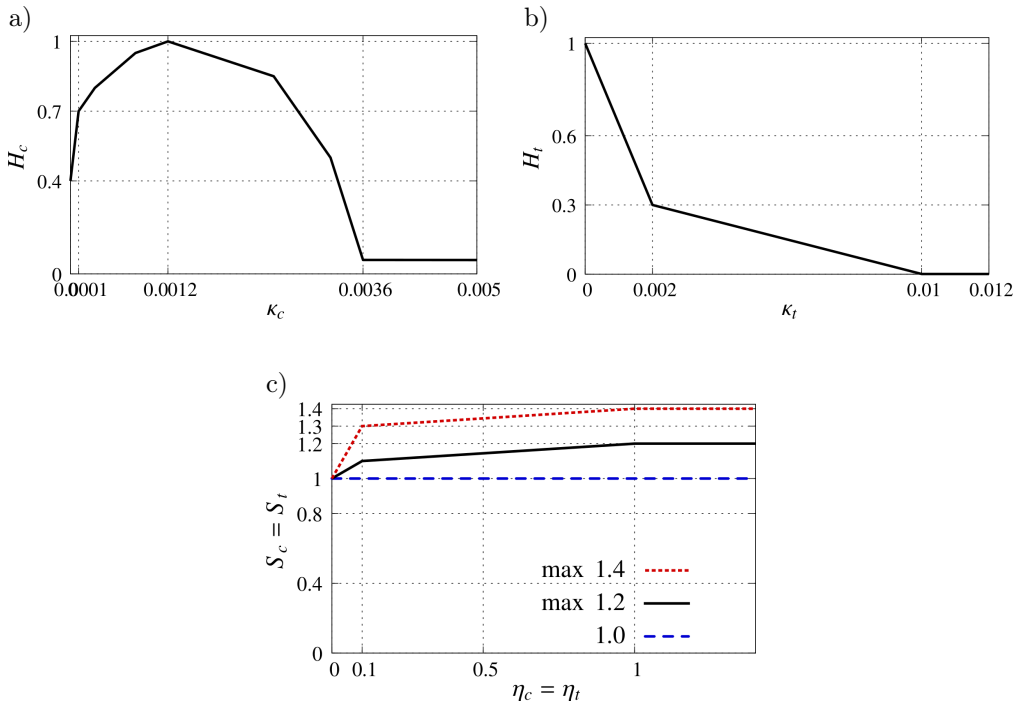


FIG. 3. Dynamic direct tension test – material functions for Hoffman viscoplasticity (HVP): a) function  $H_c$ , b) function  $H_t$ , c) functions  $S_c = S_t$ .

Analogically, function  $H_t$  in Fig. 3b dependent on the equivalent viscoplastic strain  $\kappa_t$  is determined for tension. In this benchmark for viscoplastic strain rates  $\eta_c$  and  $\eta_t$  functions  $S_c$  and  $S_t$  are identical, see Fig. 3c. It means that  $g_c = g_t = 1$  and the so-called isotropic version of the model is assumed. However, three different paths (1.0, max 1.2 and max 1.4) are employed in order to show the influence of the viscous term on the results. All functions are piecewise linear. For the GDA model, the exponential damage growth function according to Eq. (19) is introduced with threshold  $\kappa_o = 0.00188$  (tensile strength  $f'_t = 3.4$  MPa), residual stress parameter  $\alpha = 0.99$  and ductility parameter  $\eta = 500$ . The modified von Mises definition of the equivalent strain in Eq. (18) is applied with the ratio  $k = 10$ . For the GDA model, three different values of internal length scale parameter are considered, i.e.,  $l = 2/4/8$  mm, to demonstrate the effect of the gradient enhancement of the model on the results. The elastic constants for the steel reinforcement are:  $E = 200000$  MPa,  $\nu = 0.0$ . The reinforcement ratio is 1%, so the cross-section  $A_r$  is  $30 \text{ mm}^2$ . The density parameter for steel is  $\rho = 7800 \text{ kg/m}^3$ . The full bond between the concrete matrix and the reinforcement is assumed.

The diagrams depicted in Fig. 4 present the behaviour of the HVP model in two versions of the test: without and with the reinforcement, where three cases with different functions  $S_c = S_t$  are studied. When plain concrete and the classical rate-independent plasticity are analyzed, i.e., function  $S_c = S_t = 1.0$  and hence the viscous term is deactivated, then the elongation in point A tends to infinity, see the dashed line in Fig. 4a. In the case of max  $S_c = \text{max } S_t = 1.2$  viscosity activates, but still the elongation boundlessly grows even though its increase is significantly slower. The activation of the viscous term for the last case with max  $S_c = \text{max } S_t = 1.4$  is the strongest and leads to oscillations in the elongation-time diagram. Moreover, it seems that almost elastic response for plain concrete is obtained in this case. The problem becomes regularized. In contour plots of equivalent plastic strain  $\kappa_t$  two standing waves are observed

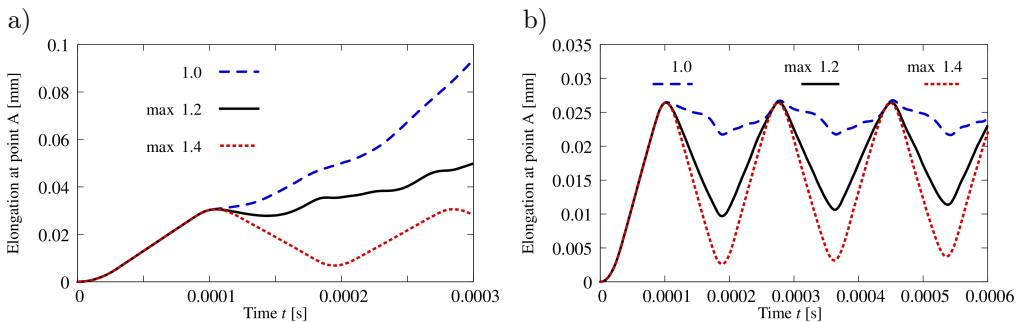


FIG. 4. Dynamic direct tension test – elongation history for Hoffman viscoplasticity (HVP), influence of viscoplastic strain rate function  $S_t$  for plain (a) and reinforced (b) concrete.

near the centre of the bar, cf. Figs 5a and 5b. The two separated zones of localization are probably an artificial numerical effect. The simulation result with one central zone is consistent with the analytical solution for the strain-softening bar presented in [3], where the standing decohesion wave is located exactly in the centre. Figure 5c depicts one wider cracked zone for the case with  $\max S_c = \max S_t = 1.4$ .

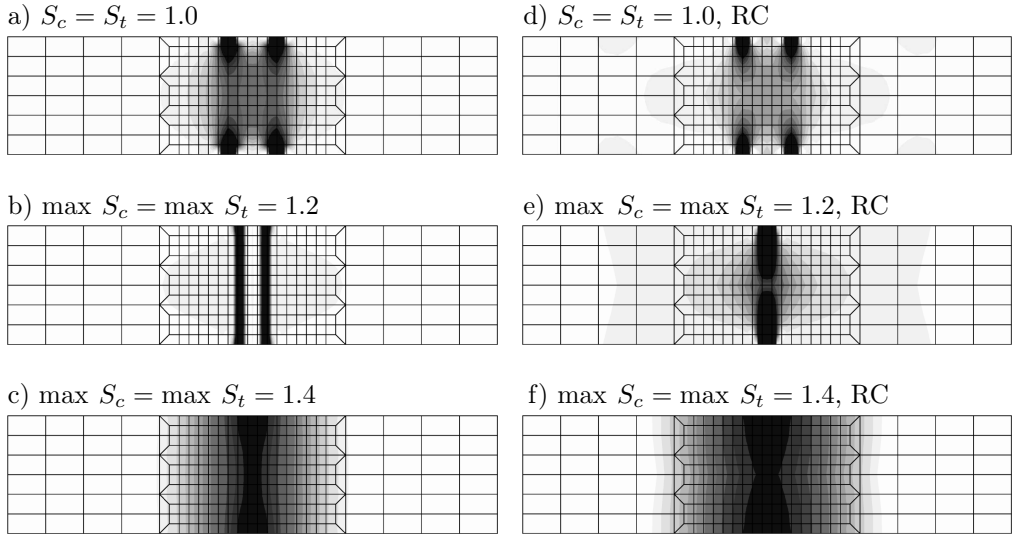


FIG. 5. Dynamic direct tension test – distribution of equivalent plastic strain for tension  $\kappa_t$  for the HVP model in  $t = 0.0003$  s, influence of function  $S_c = S_t$  for plain (a–c) and reinforced (d–f) concrete.

In general, the presence of the reinforcement partly stops the process of localization, and the horizontal displacement at point A oscillates around a certain state, cf. diagrams in Fig. 4b. The contour plot for RC and  $S_c = S_t = 1.0$  shown in Fig. 5d looks similar to the distribution for plain concrete in Fig. 5a, so in that case, the detached zones are also visible for the configuration with the reinforcement. However, more diffuse crack patterns are noticed when the viscous term is activated, see Figs 5e and 5f. It is seen that the viscous term in the HVP model plays an important role and the increase of function  $S_c = S_t$  can favorably affect the global response of dynamic direct tension. All contour plots are prepared for the time instant  $t = 0.0006$  s (after 300 time steps).

Figure 6 presents the internal length influence for the GDA model in the case of plain and reinforced concrete. Analogous to the regularization via the viscous term in the HVP model, the elongation-time diagrams in Fig. 6a for plain concrete show that the smaller the value of the internal length parameter  $l$  is, the faster the elongation at point A goes to infinity. It is shown in Fig. 6b that for

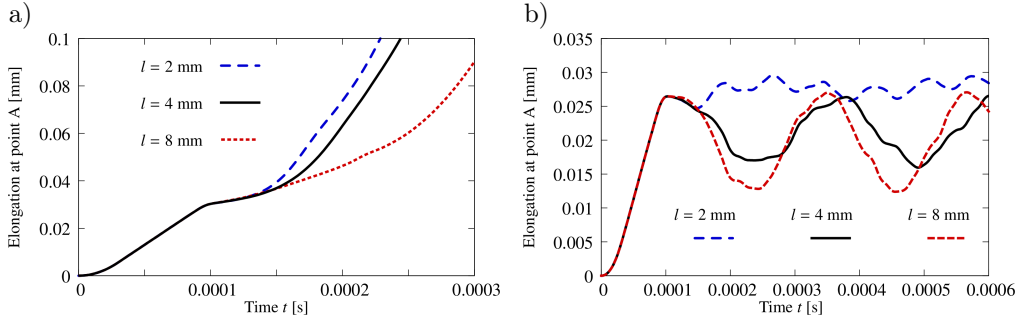


FIG. 6. Dynamic direct tension test – elongation history for gradient damage (GDA), influence of internal length parameter for plain (a) and reinforced (b) concrete.

the RC bar and the case with small  $l = 2$  mm, the amplitude of elongation during vibrations is significantly smaller than for larger  $l$ . If the gradient-enhanced activity is stronger ( $l = 4$  or 8 mm), then the regularization is more effective. In fact, similar behaviour is observed for the HVP model with the viscous active viscus term. Figure 7 demonstrates contour plots of the averaged strain obtained using the GDA model for plain and reinforced concrete.

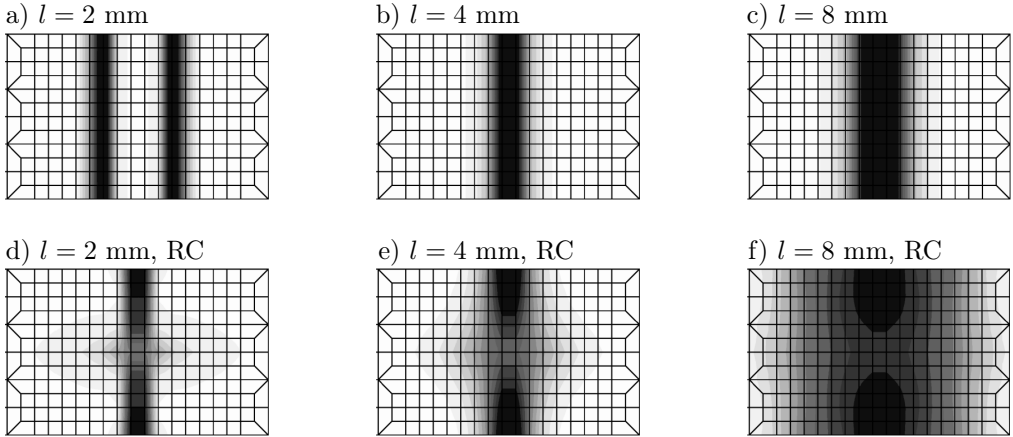


FIG. 7. Dynamic direct tension test – distribution of averaged strain  $\bar{\epsilon}$  for the GDA model in  $t = 0.0003$  s, influence of internal length parameter for plain (a-c) and reinforced (d-f) concrete.

The general tendency for both models is that the width of the localization zone increases with larger influence of the regularizing term, but the reinforcement additionally delays the progress of cracking along the whole bar height. The assumption of the full bond between steel and concrete leads to an underestimation of localization in the closest neighbourhood of the reinforcement. A proper

representation of bond-slip, together with the implementation of interface elements, can reproduce the width of the localization zone in a more realistic way (see, e.g., [45, 47, 56]), but it is out of the scope of the paper. The presence of the reinforcement in this benchmark is mainly supposed to suppress the evolution of the localized zone. In fact, its presence also regularizes the problem. It should also be mentioned that for a non-zero Poisson's ratio the crack patterns look similarly to the ones presented above.

### 3.2. Cylinder split test

The next example presents the simulation of a cylinder specimen under compressive impact loading through bearing strips. This experiment is called in the literature a split or Brazilian test, see, e.g., [19, 44, 46], and is commonly used to establish the tensile strength for concrete, rock and other quasi-brittle materials [9]. The compression between the loading platens induces a perpendicular tensile force in the middle of the cylinder, which can induce primary and secondary cracks. Finally, splitting inside the specimen is observed. The idea of the laboratory test is shown in Fig. 8a. Plane strain conditions are adopted for the computations, but the split test can also be modelled as a fully three-dimensional specimen [46] or as a disc for plane stress conditions [69]. The results obtained by the authors for the split test under static loading are discussed in [72]. Here the radius of the cylinder is 25.4 mm. The input data are similar to [46], where the specimen is made of plain concrete with the maximum aggregate size equal to 8.5 mm, cf. also the experiment in [59]. Due to double symmetry only a quarter of the domain is considered. Three mesh refinements are compared. In Fig. 8b the medium mesh with the load scheme is depicted. Eight-noded FEs are applied as in the computations for direct tension test. For the GDA model, quadratic/linear interpolation is applied. The influence of the platens, presence on the numerical solution is shown in [72] and here this aspect is omitted.

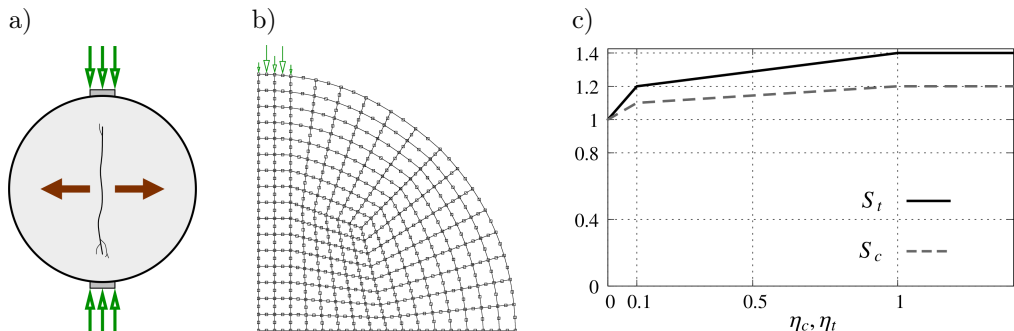


FIG. 8. Split test – problem definition: a) idea of test, b) medium mesh, c) functions  $S_c$  and  $S_t$  for the HVP model.

The fundamental material data for concrete are: Young's modulus  $E = 37900$  MPa, Poisson's ratio  $\nu = 0.15$ , density  $\rho = 2405$  kg/m<sup>3</sup>. The linear-constant type of pulse loading is introduced according to Fig. 2b, but now the traction intensity  $p_i = 175$  MPa is reached for time instant  $t_i = 48$   $\mu$ s. The impact of different loading rates (various instants  $t_i$ ) on the numerical response is also studied. The time step is 1  $\mu$ s. For the HVP model initial tensile strength  $f'_t$  equals 4.53 MPa and initial compressive strength  $f'_c$  is equal to 67 MPa. Functions  $H_c$  and  $H_t$  are the same as in the previous section, see Figs 3a and 3b, respectively. Functions  $S_c(\eta_c)$  and  $S_t(\eta_t)$  are defined here according to Fig. 8c, so nonisotropic behaviour of the consistency model and  $\kappa_c \neq \kappa_t$  are taken into account (see details in [68]). When the GDA model is considered, then exponential softening defined in Eq. (19) is employed with threshold  $\kappa_o = 0.00011953$  (i.e., tensile strength  $f'_t$  is 4.53 MPa) and parameters  $\alpha = 0.98$  and  $\eta = 600$ . Again, the modified von Mises definition of damage loading function via Eq. (18) with the ratio  $k = 14.79$  (compressive strength  $f'_c = 67$  MPa) is selected. The internal length scale  $l$  is 4 mm.

Firstly, the results for the HVP model are discussed. The vertical displacement  $v(t)$ , velocity  $V(t)$  and acceleration  $a(t)$  for a point at the top of the quarter of the considered domain are shown in the history diagrams in Fig. 9.

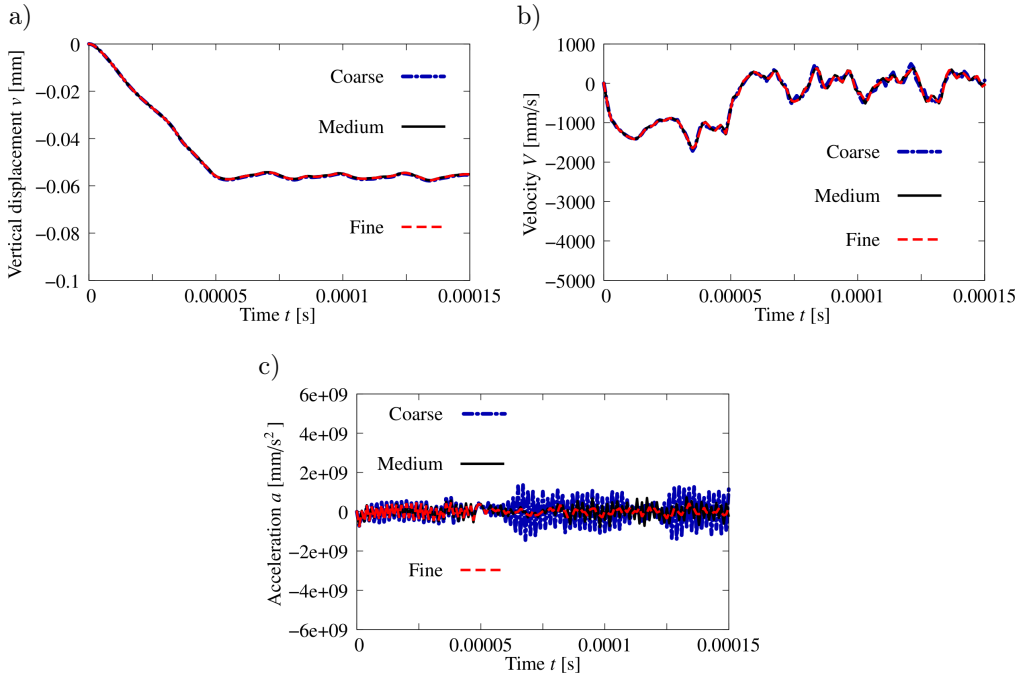


FIG. 9. Split test – response histories for the HVP model, three different mesh densities: a) displacement history, b) velocity history, c) acceleration history.

The functions of displacement  $v$  and velocity  $V$  are almost independent of the discretization, while acceleration  $a$  differs especially for the coarse mesh, but that effect is known in numerical analyses of dynamics. Figures 10–12 illustrate in a sequence the distributions of strain component  $\varepsilon_{11}$ , equivalent plastic strain for compression  $\kappa_c$  and for tension  $\kappa_t$  for three employed meshes in two selected time instants, namely  $t = 50 \mu\text{s}$  and  $150 \mu\text{s}$ . The first time instant is just after loading changes from linear to constant, and the second one is the final time on the diagrams. It is observed for all the plots that almost the same distributions for respective variables are obtained independently of the mesh. For strain  $\varepsilon_{11}$  at  $t = 50 \mu\text{s}$  in Fig. 10, the split zone arises from the center of the area along the vertical symmetry axis, but at  $t = 150 \mu\text{s}$  the maximum strain moves up. The distribution of internal variable  $\kappa_c$  in Fig. 11 is concentrated at the top, i.e., at under the place where the load presses the specimen and where the largest compression occurs. On the other hand, contour plots in Fig. 12 show that tensile cracking is present near the centre adequately for the beginning of the split process. For instant  $t = 150 \mu\text{s}$  maximum tensile equivalent plastic strains  $\kappa_t$  are still there, but only the zone of maximum values becomes wider.

The next aspect of the study is the influence of different loading rates. The computations are performed for the medium mesh. Three options are considered for different instants  $t_i$  after which the loading becomes constant. Each

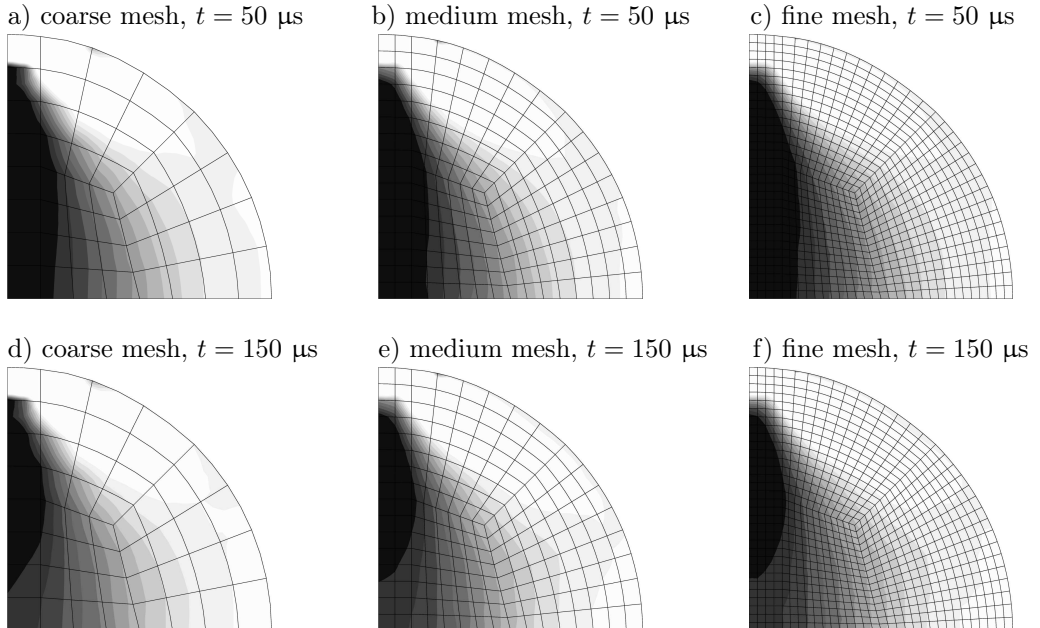


FIG. 10. Split test – the HVP model, distribution of strain  $\varepsilon_{11}$  for three different meshes in two selected time instants.

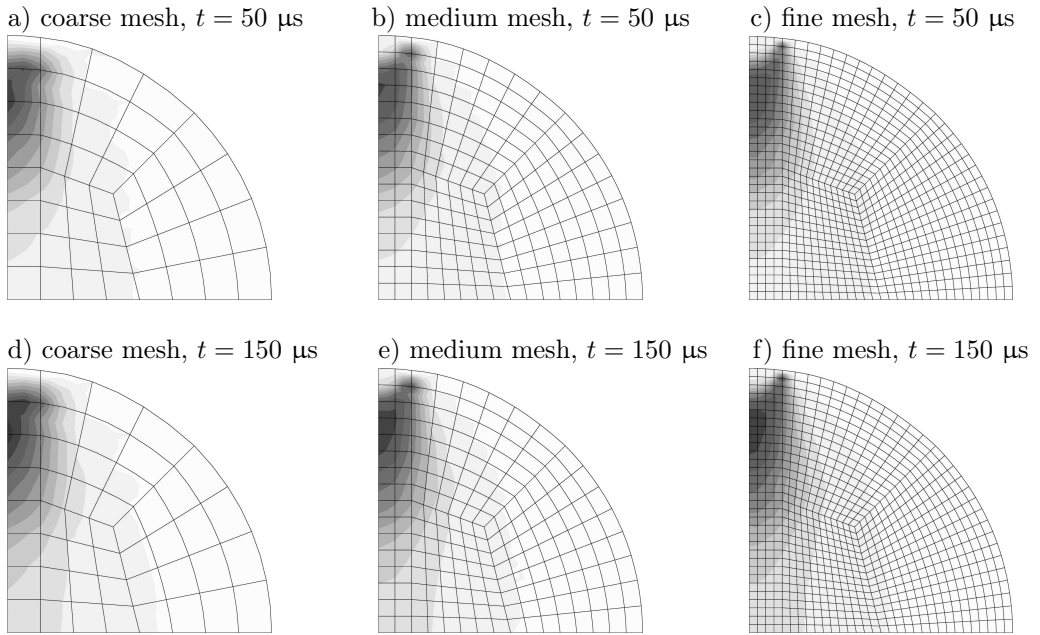


FIG. 11. Split test – the HVP model, distribution of equivalent plastic strain for compression  $\kappa_c$  for three different meshes in two selected time instants.

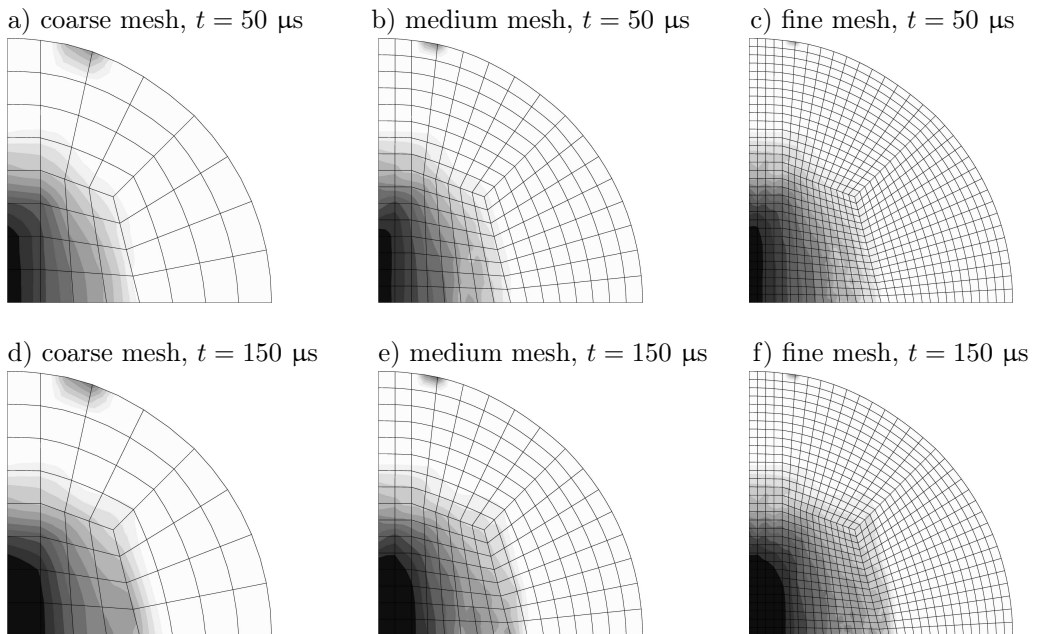


FIG. 12. Split test – the HVP model, distribution of equivalent plastic strain for tension  $\kappa_t$  for three different meshes in two selected time instants.

displacement-time diagram plotted in Fig. 13a is similar to the linear-constant function and is associated with the given load  $p(t)$ , see also Fig. 2b. Only the slope of the first part of the diagrams differs. Slight variations are noticed in Fig. 13b for velocity, where values of each graph go back to near-zero oscillations for about  $t_i = 40 \mu\text{s}$ ,  $t_i = 48 \mu\text{s}$  and  $t_i = 56 \mu\text{s}$ , respectively to the instant of the change of the loading. Figure 13c demonstrates the acceleration history.

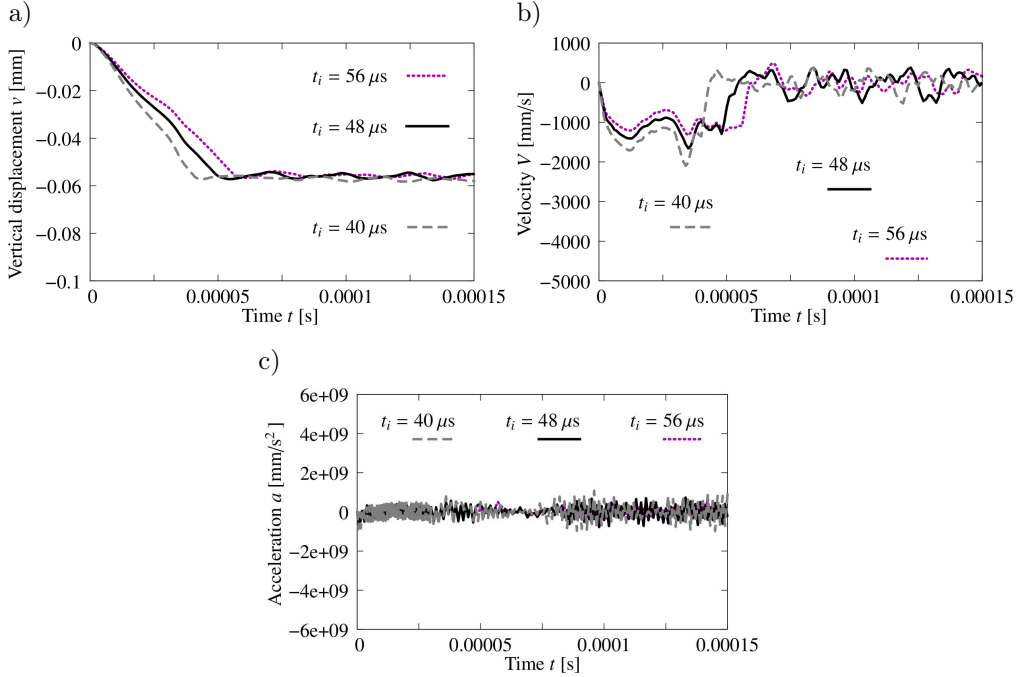


FIG. 13. Split test – response histories for the HVP model, medium mesh, three different loading rates: a) displacement history, b) velocity history, c) acceleration history.

Figure 14 represents distributions of  $\epsilon_{11}$ ,  $\kappa_c$  and  $\kappa_t$  at time instant  $t = 150 \mu\text{s}$  for the case  $t_i = 40 \mu\text{s}$ . Corresponding contour plots for the case  $t_i = 56 \mu\text{s}$  are

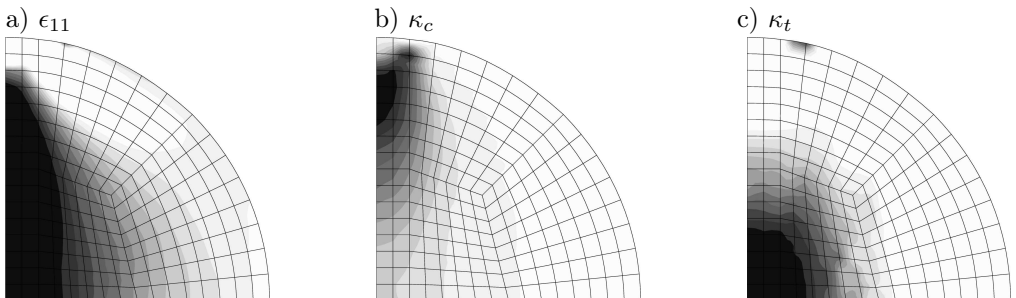


FIG. 14. Split test – contour plots for the HVP model, medium mesh, case  $t_i = 40 \mu\text{s}$ , time instant  $t = 150 \mu\text{s}$ .

shown in Fig. 15. More intense patterns are visible for  $t_i = 40 \mu\text{s}$ . The adopted values of the process speed make the viscous term sufficiently active and quite spread distributions are observed. On the other hand, the rapidness of the loading is not strong enough to cause too early failure of the specimen or even numerical divergence in the analysis. The influence of this speed is discussed in [68] and evident diversities in the response of viscoplastic models are detected if values of the loading rate differ by a few orders. The splitting analysis in this respect, but for statics, is also presented in [72].

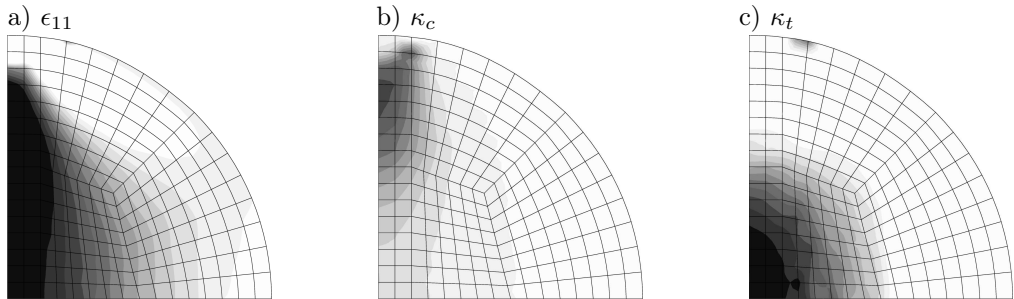


FIG. 15. Split test – contour plots for the HVP model, medium mesh, case  $t_i = 56 \mu\text{s}$ , time instant  $t = 150 \mu\text{s}$ .

The last part of this subsection is devoted to the description of the results for the GDA model. The layout of this presentation is identical as for the HVP model. The diagrams in Fig. 16 are depicted for three different meshes, again for the histories of vertical displacement  $v$ , velocity  $V$  and acceleration  $a$ . The point at the top of the specimen quarter is taken into consideration. It is noticeable that the responses for the coarse mesh slightly deviate from the other paths. It is also clear that the total failure of the specimen is more or less at time instant  $t = 90 \mu\text{s}$ . Hence, Figs 17–19 are prepared for two characteristic time instants. Time  $t = 50 \mu\text{s}$  is selected due to change of the loading and  $t = 90 \mu\text{s}$  is when the progressive failure is significantly advanced. Distributions of strain  $\epsilon_{11}$  are analogous to the ones presented for the HVP model, but the zone of maximum strains slightly broadens. Surprisingly, along the circumference away from the applied load, a small area of significant strains is observed. At this place, tensile cracking is likely and can be interpreted as the beginning of a wedging effect. In Fig. 18, the contour plots of the averaged strain measure  $\bar{\epsilon}$  (ASM) are illustrated for  $t = 50 \mu\text{s}$  and almost the same distributions are observed. Therefore, mesh independence and the presence of the regularization effect seem obvious. However, different distributions are obtained for  $t = 90 \mu\text{s}$ . A concentration directly below the loading where the specimen is compressed is particularly reflected for the coarse mesh, see Fig. 18d. This effect vanishes for the fine mesh, cf. Fig. 18f. Such difference can be explained by the fact that time  $t = 90 \mu\text{s}$  is just before the

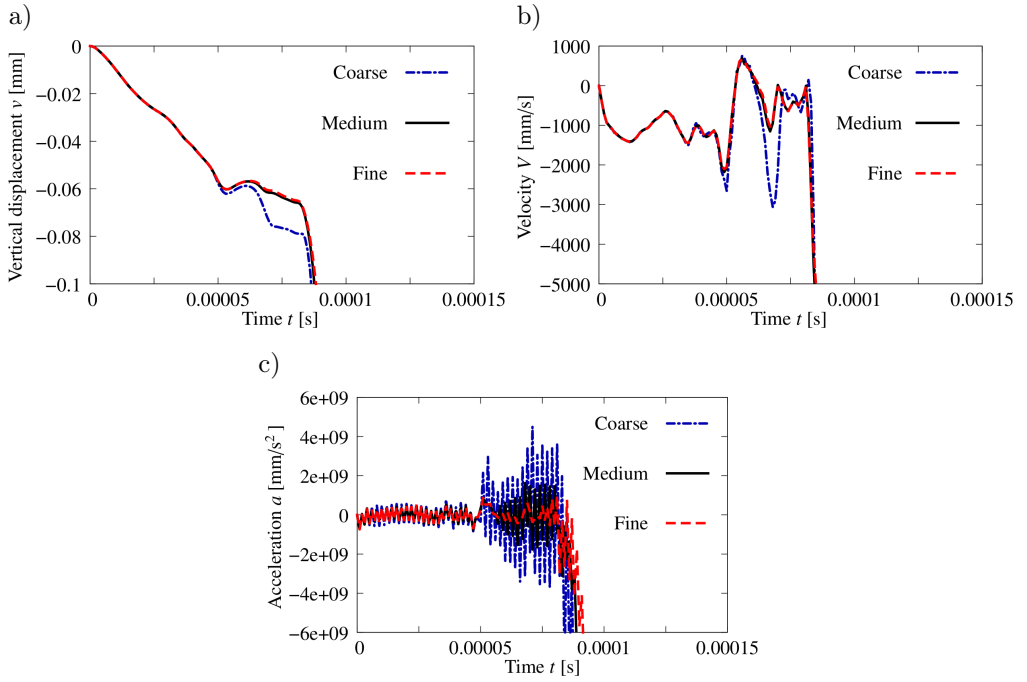


FIG. 16. Split test – response histories for the GDA model, three different mesh densities: a) displacement history, b) velocity history, c) acceleration history.

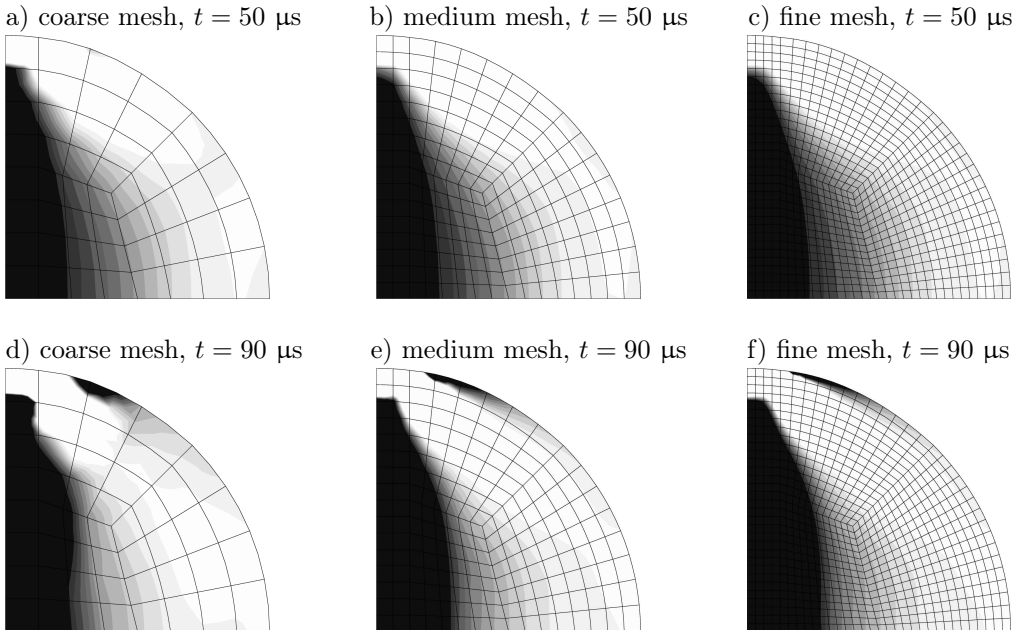


FIG. 17. Split test – the GDA model, distribution of strain  $\epsilon_{11}$  for three different meshes in two selected time instants.

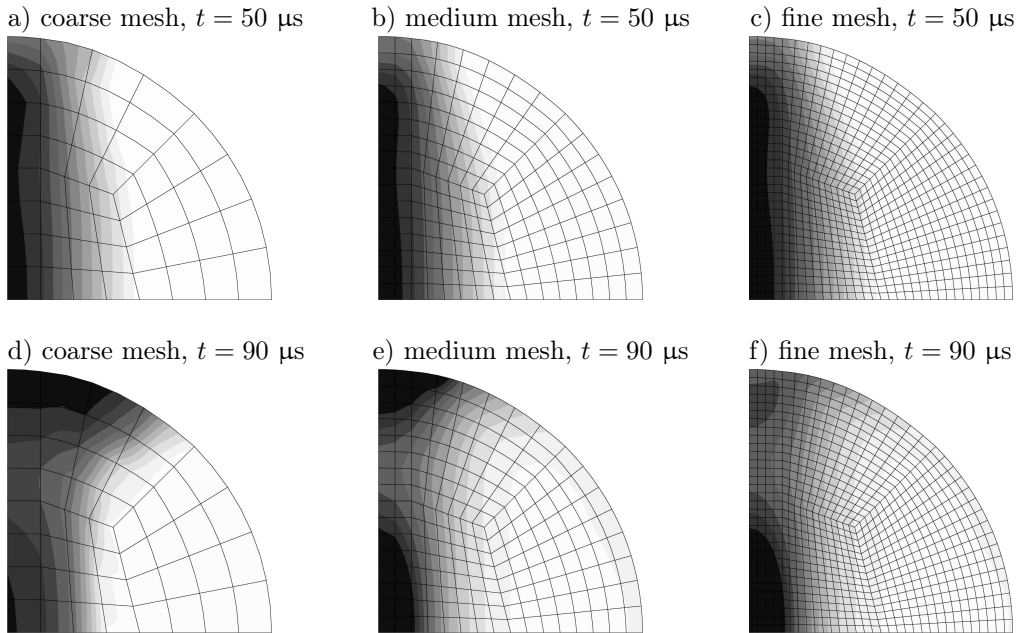


FIG. 18. Split test – the GDA model, distribution of averaged strain measure  $\bar{\epsilon}$  for three different meshes in two selected time instants.

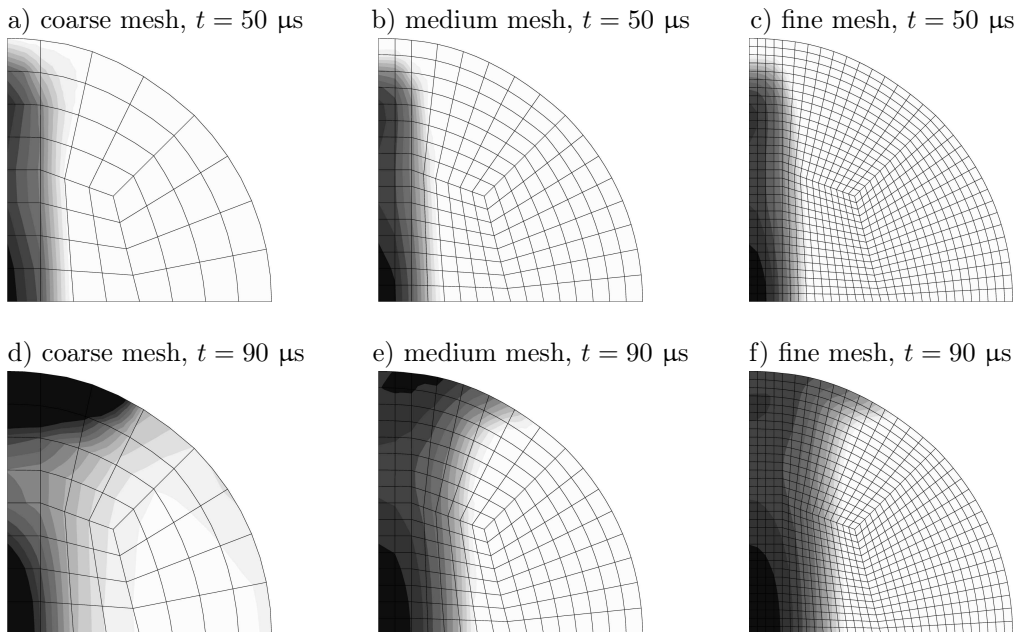


FIG. 19. Split test – the GDA model, distribution of damage  $\omega$  for three different meshes in two selected time instants.

failure. Damage patterns in Fig. 19 are corresponding to the ASM distributions. The damage zones for time instant  $t = 50 \mu\text{s}$  seem to be very narrow. It should be noted that for  $t = 50 \mu\text{s}$  the maximum damage  $\omega$  equals 0.30, while for  $t = 90 \mu\text{s}$  the maximum damage  $\omega$  reaches about 0.95. Again, the zone below the loading is visible for the coarse mesh at time  $t = 90 \mu\text{s}$ . Damage patterns can be treated as a continuum representation of cracking, so it can be concluded that the splitting in the central vertical zone is simulated correctly by the GDA model.

Similarly to the results of the HVP model, the importance of loading rates is next analyzed for the GDA model. In this study, the medium mesh is only considered. Three different time instants when the load changes from linear to constant are investigated:  $t_i = 40 \mu\text{s}$ ,  $t_i = 48 \mu\text{s}$  and  $t_i = 56 \mu\text{s}$ . The displacement history is represented in Fig. 20a. The absolute values of vertical displacement  $v$  suddenly tend to infinity for the case  $t_i = 40 \mu\text{s}$ , i.e., for the largest loading rate. It means that the most rapid failure emerges. On the other hand, for the case  $t_i = 56 \mu\text{s}$  oscillations continue till instant  $t = 130 \mu\text{s}$ . This phenomenon is also observed in the diagrams in Figs 20b and 20c for velocity and acceleration. The slower the loading rate is, the longer time to total failure is simulated. For the GDA model, the characteristic variables are also plotted in Figs 21 and 22,

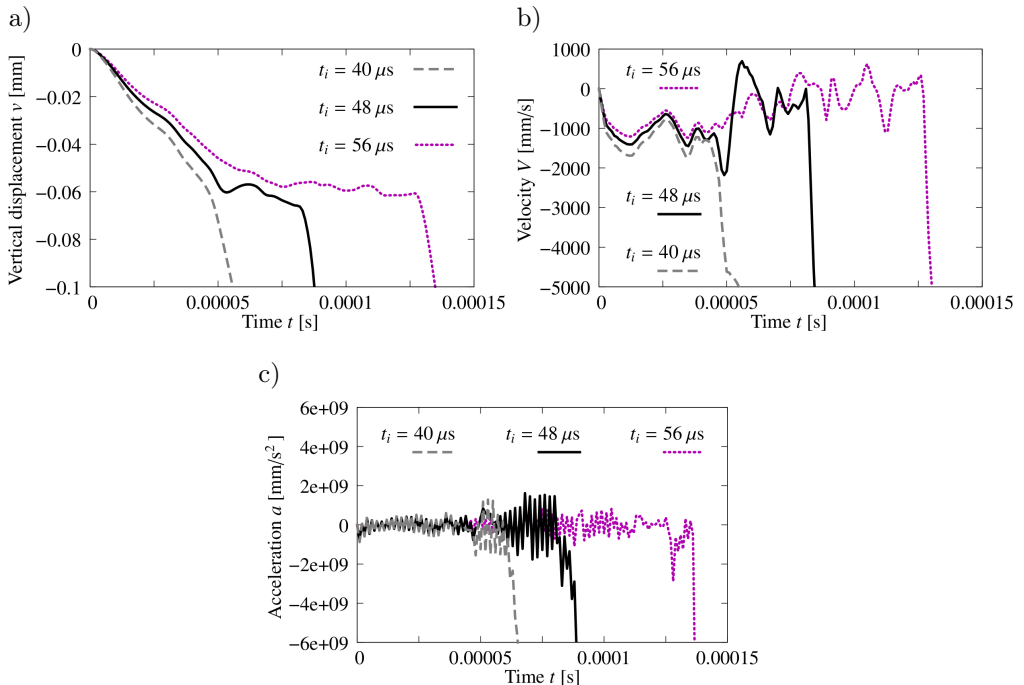


FIG. 20. Split test – response histories for the GDA model, medium mesh, three different loading rates: a) displacement history, b) velocity history, c) acceleration history.

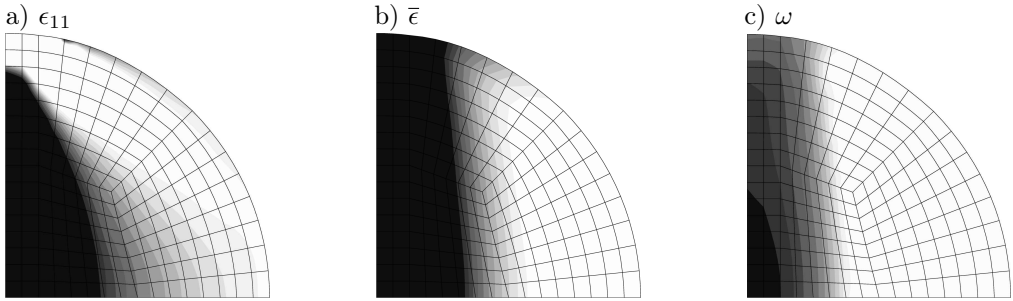


FIG. 21. Split test – contour plots for the GDA model, medium mesh, case  $t_i = 40 \mu\text{s}$ , time instant  $t = 55 \mu\text{s}$ .

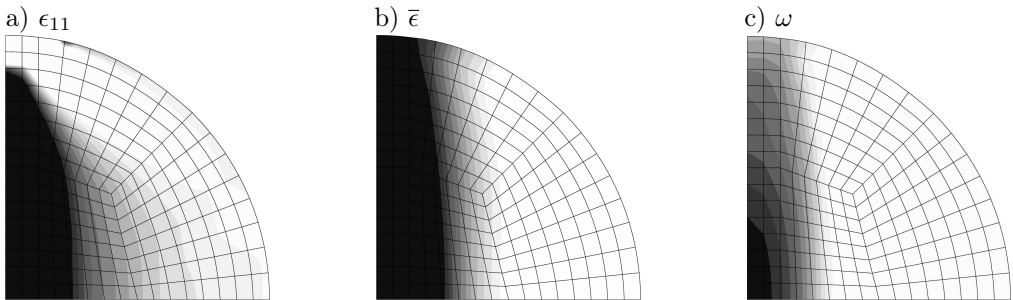


FIG. 22. Split test – contour plots for the GDA model, medium mesh, case  $t_i = 56 \mu\text{s}$ , time instant  $t = 130 \mu\text{s}$ .

namely: strain component  $\varepsilon_{11}$ , averaged strain  $\bar{\varepsilon}$  and damage  $\omega$ . For the case  $t_i = 40 \mu\text{s}$ , the final time before failure is  $t = 55 \mu\text{s}$  and in Fig. 21 this moment is captured. Generally, the crack patterns are similar to the previous results of the GDA model (case  $t_i = 48 \mu\text{s}$ ), but the distribution of ASM is much more intense, see Fig. 21b. The contour plots in Fig. 22 for  $t_i = 56 \mu\text{s}$  are taken when  $t = 130 \mu\text{s}$  (final moment). The type of the corresponding distributions remains generally unchanged, but the crack zones are a little narrower. Here the GDA model is very sensitive to the loading rate, opposite to the HVP model where just high loading rates can modify the response, cf. [68, 72].

### 3.3. Four-point bending

This benchmark is referred to a reinforced concrete (RC) beam, which was tested experimentally under dynamic loading and then described in [18]. The other computations for this configuration using various cracking descriptions are presented in [16, 55].

The data are set on the basis of [55]. The geometry is illustrated in Fig. 23a. Two supports are placed at the bottom of the beam, while two dynamic forces

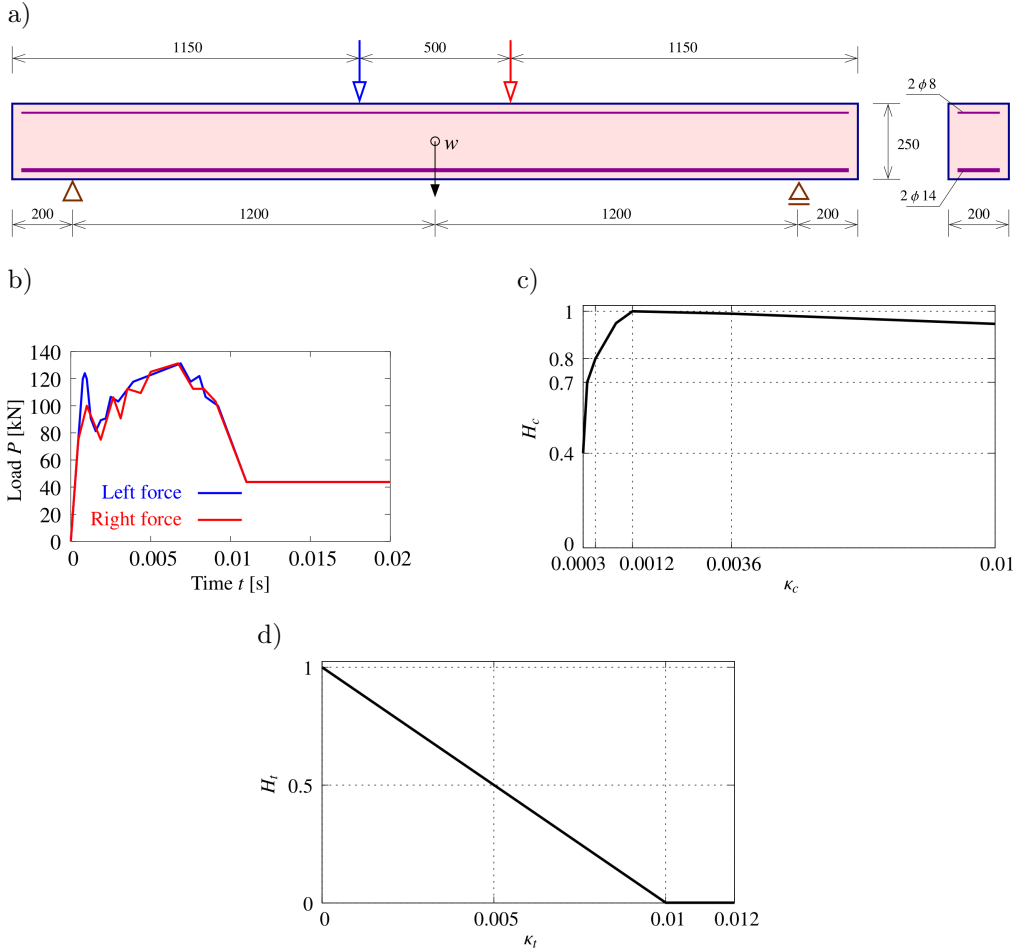


FIG. 23. Four-point bending – problem definition: a) geometry (dimensions in mm), b) load history, c) function  $H_c$  for HVP, d) function  $H_t$  for HVP.

are imposed at two points at the top. The beam is loaded by impact as in the experiment [18], with slightly different load histories, as shown in Fig. 23b. Despite the above fact, the experimental history for the beam centre deflection was presented in [18] up to time  $t = 0.006$  s. The load control, plane stress conditions as well as full bond between steel and concrete are assumed. These computations are performed for three different FE meshes for the concrete matrix, namely: coarse –  $56 \times 8$ , medium –  $112 \times 16$  and fine –  $168 \times 24$  elements. Quadrilateral FEs are applied, linear interpolation is adopted for both fields in the GDA model, see also [41]. It is known that although quadratic/linear interpolation is optimal for gradient models, the other possibilities can give stable results as well, see, e.g., [72], since this model is coupled rather than mixed. It is

mentioned in [49] that the so-called inf-sup condition does not have to be obeyed. Oscillations that may occur for some secondary fields, e.g., stress components, have local character and are visible only in the neighbourhood of strong damage variation. In the experiment, concrete was extra reinforced by steel fibers (1.2% volume), so it motivates additionally the presence of regularization in the material model. Moreover, ductility should also be increased. The basic data for concrete are the following: Young's modulus  $E_c = 32940$  MPa, Poisson's ratio  $\nu_c = 0.2$ , density  $\rho = 2320$  kg/m<sup>3</sup>, tensile strength  $f'_t = 3.15$  MPa and compressive strength  $f'_c = 10f'_t$ . Steel is modelled as elastic-ideal-plastic material in uniaxial stress state using truss finite elements. Lower reinforcement is located at 31.25 mm from the bottom, and two bars with the diameter  $\phi = 14$  mm give the cross-section area  $A_{sb} = 308$  mm<sup>2</sup>. Upper reinforcement is located at 31.25 mm from the top, and now two bars with the diameter  $\phi = 8$  mm correspond to the area  $A_{st} = 100.5$  mm<sup>2</sup>. The other data for steel are: Young's modulus  $E_s = 245390$  MPa, Poisson's ratio  $\nu_s = 0.3$ , density  $\rho = 7800$  kg/m<sup>3</sup> and yield strength  $f_y = 638$  MPa.

Piecewise linear functions  $H_c$  and  $H_t$  depicted in Figs 23c and 23d are adopted for the HVP model. It should be noticed that now ductility of the concrete model is increased in comparison to both previous examples, especially in the compression regime. As shown in [72], the HVP model can be sensitive to the definition of  $H_c$ . The presence of fibers in the concrete matrix can partly explain the increased ductility for tension, but the numerical divergence is prevented as well. Functions  $S_c$  and  $S_t$  are identical as in the split test, see Fig. 8c. The viscoplastic strain rate grows differently for compression and tension, hence the nonisotropic variant of the HVP model is considered (see details in [68]). The parameters of the GDA model are: threshold  $\kappa_o = 95.6 \times 10^{-6}$ , the exponential softening function given in Eq. (19) with  $\alpha = 0.96$  and  $\eta = 350$ , the modified von Mises definition in Eq. (18) with  $k = 10$  and the internal length scale  $l = 16$  mm. It is emphasized that here only the results for the medium mesh, coming from this model, are recalled to make the background for the computations using the HVP model. The full analysis of four-point bending for the GDA was originally performed and widely described in [71], including also the results for statics with different aspects of the model. Moreover, in [39] the benchmark is computed by means of so-called stabilized finite elements to show the application of hourglass control in two-field finite elements for the GDA model.

The experimental path for deflection  $w$  in the center of the beam is taken from [18]. All the computed deflection histories, shown in Fig. 24a, demonstrate a quite good agreement with the experimental response. Furthermore, the independence of the discretization is observed for the diagrams obtained for the HVP model. Figures 24b and 24c are prepared based on the computations only and illustrate the velocity and acceleration histories. Again, the velocity plots for the HVP

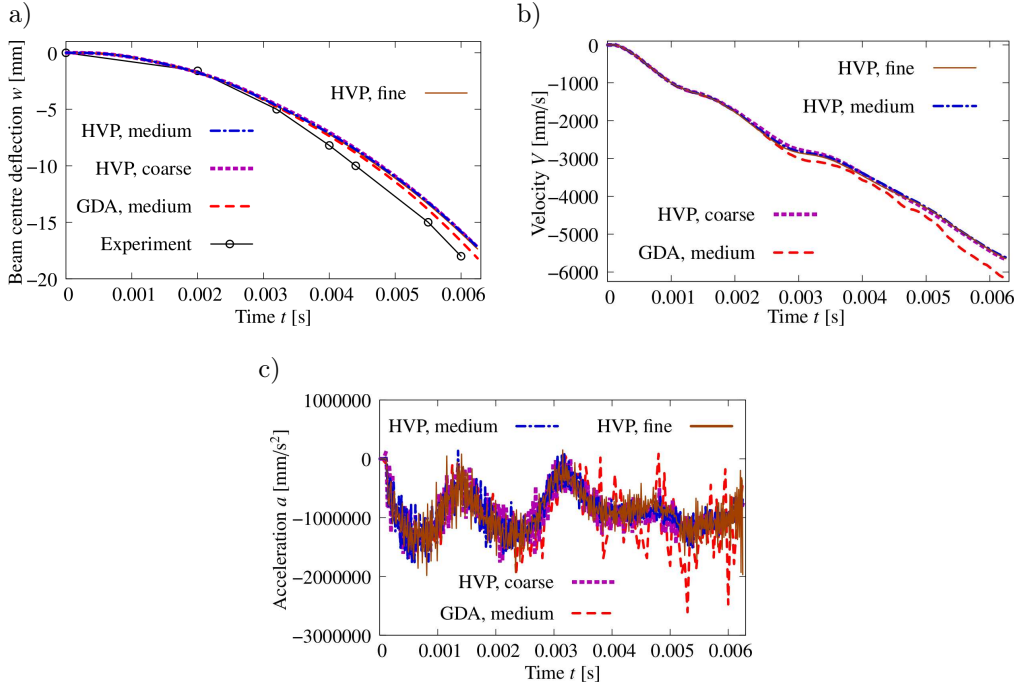


FIG. 24. Four-point bending – response histories, three different meshes:  
a) displacement history, b) velocity history, c) acceleration history.

model are almost the same for all meshes and the difference with reference to the GDA model is really small. The absolute values of velocity rise permanently, and this can be interpreted as a tendency of the RC beam to failure. Although the character of acceleration histories shown in Fig. 24c looks similar to previous tests, the response is more sensitive to the employed discretization. However, the most extreme amplitudes are distinguished for the GDA model.

In Fig. 25, the next results for the HVP model are shown, i.e., the distribution of equivalent plastic strain for tension  $\kappa_t$  and deformation for three different meshes in final  $t = 0.00625$  s. At this time instant, the computations are intentionally interrupted. Unfortunately, some mesh dependence occurs. For the coarse mesh, the distribution of  $\kappa_t$  presented in Fig. 25a shows too diffused cracking, while for the medium and fine meshes in Figs 25c and 25e two clear localization zones are visible with the same intensity and in the same range of damage (black colour). Deformations presented in Figs 25b, 25d and 25f are in accordance with the plastic hinges theory. Nevertheless, a so-called “elephant foot” (excessive dilatation) phenomenon can be visible, particularly for the deformation of the fine mesh, see Fig. 25f. This is an undesirable numerical effect that is observed when the model with the associated plastic flow is computed. This issue could be removed by the implementation of nonassociated flow rule in

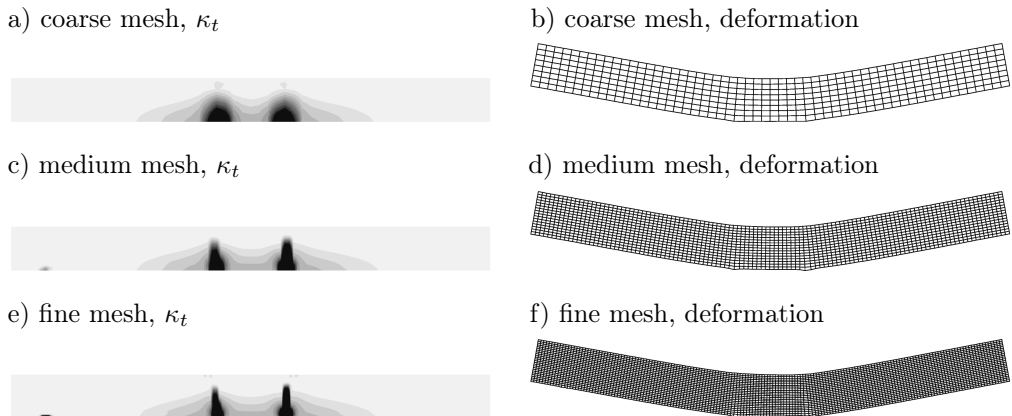


FIG. 25. Four-point bending – the HVP model, distribution of equivalent plastic strain for tension  $\kappa_t$  and deformation for three different meshes in  $t = 0.00625$  s.

the HVP model. Figure 26 presents the distribution of averaged strain measure  $\bar{\epsilon}$  and deformation selected only for the medium mesh obtained for the GDA model (they are just plotted for comparison, the other results can be found in [71]). It is seen that in the case of the medium mesh the corresponding distributions for both models are quite similar, but deformation in Fig. 26b for the GDA model at the location of the most intensive cracking displays rather a concavity of the deformed mesh (local volume decrease), and not a convexity – as in the HVP model.

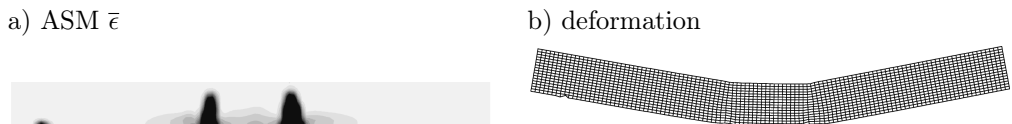


FIG. 26. Four-point bending – the GDA model, distribution of averaged strain  $\bar{\epsilon}$  and deformation for medium mesh in  $t = 0.00625$  s.

#### 4. SUMMARY AND CONCLUSIONS

In this paper, the theory of two regularized models for concrete has been reviewed. The Burzyński-Hoffman viscoplastic consistency model (HVP) incorporates separate rate-dependent functions for compression and tension to describe the nonlinear behaviour of the material. In this concept, the viscous term provides the rate localization limiter dependent on a time scale. The model has been implemented in the FEAP code as a usermat subroutine. For dynamics, the standard Newmark algorithm is applied. The gradient damage model (GDA) incorporates the simplified representation of sensitivity to strain sign via a corre-

sponding equivalent strain measure. The model can be coupled to plasticity [14]. Spatial gradients of strain ensure the differential limiter dependent on an internal length scale. For this model, a user-element subroutine has been implemented because of the two-field formulation. The independent averaged strain field was also interpolated, together with the displacement field, but the problem is coupled and not mixed. Hence, the uniform interpolation of the two fields can be used. For dynamics, the mass matrix has to be defined in order to correctly approximate the initial boundary value problem (IBVP). Again, the standard Newmark algorithm was employed.

Three concrete dynamic benchmarks have been analyzed. The influence of the regularizing term was demonstrated for both models in the direct tension test.

The width of the localization zone increased in accordance with stronger regularization resulting from the corresponding model data: functions dependent on the viscoplastic strain rate for the HVP model and the internal length scale parameter for the GDA model. The localization limiters slowed down the elongation of the specimen. As expected, the progress of the cracking phenomenon was delayed or obstructed by the presence of the reinforcement.

It was further shown that the splitting effect under impact loading is quite well reproduced using both models. The results are independent of discretization density. It turns out that in the case of the coarse mesh for the GDA model the distributions of averaged strain  $\bar{\epsilon}$  and damage  $\omega$  differed from the others at the final time. It is possible that the discretization was too coarse or simply the crack patterns immediately before failure could be different. The influence of loading rates was also studied, and obviously, the faster the pulse is, the more violent cracking occurs.

Finally, simulations of the dynamic four-point bending according to the experiment [18] were performed. A quite good agreement between the results for both models was noticed. The patterns obtained in the computations look realistic and have a physical interpretation in accordance with the plastic hinges theory. Moreover, the experimental path for the deflection at the center of the beam is also compatible with the numerical response. When the HVP model is employed the so-called “elephant foot” phenomenon can occur. This unwanted effect could be reduced if the nonassociated plastic flow was applied. This is a future task for the authors to solve this problem by the implementation of a separate plastic potential function.

Summarizing, the influence of regularization is visible in both models. The width of the standing (localization) wave is controlled by the viscosity (the rate limiter) or the internal length scale (the differential limiter). The well-posedness of the IBVP, together with its hyperbolic character, can be preserved. Owing to the regularization in the HVP and GDA models, the FE analyses of concrete

specimens under impact loading presented in this paper exhibit negligible mesh-sensitivity for sufficiently dense discretizations.

## APPENDIX.

### FINITE ELEMENT IMPLEMENTATION FOR GRADIENT DAMAGE

Certain domain  $\mathcal{B}$  occupied by a material body with boundary  $\partial\mathcal{B}$  is analyzed. The weak form of equations of motion (1) using standard boundary conditions is as follows:

$$\int_{\mathcal{B}} \delta \boldsymbol{\epsilon}^T \boldsymbol{\sigma} \, dV + \int_{\mathcal{B}} \delta \mathbf{u}^T \rho \ddot{\mathbf{u}} \, dV = \int_{\mathcal{B}} \delta \mathbf{u}^T \mathbf{b} \, dV + \int_{\partial\mathcal{B}} \delta \mathbf{u}^T \mathbf{t} \, dS, \quad (23)$$

where the superscript T is the transpose symbol and  $\mathbf{t}$  is the traction vector. The averaging equation (20) using non-standard natural boundary condition is rewritten as:

$$\int_{\mathcal{B}} \delta \bar{\boldsymbol{\epsilon}} \bar{\boldsymbol{\epsilon}} \, dV + \int_{\mathcal{B}} (\nabla \delta \bar{\boldsymbol{\epsilon}})^T c \nabla \bar{\boldsymbol{\epsilon}} \, dV = \int_{\mathcal{B}} \delta \bar{\boldsymbol{\epsilon}} \tilde{\boldsymbol{\epsilon}} \, dV. \quad (24)$$

The primary fields are interpolated in this manner:

$$\mathbf{u} = \mathbf{N} \mathbf{a} \quad \text{and} \quad \bar{\boldsymbol{\epsilon}} = \mathbf{h}^T \mathbf{e}. \quad (25)$$

After the linearization for the implicit time integration, the equations of motion become:

$$\int_{\mathcal{B}} \mathbf{B}^T (\boldsymbol{\sigma}^t + \Delta \boldsymbol{\sigma}) \, dV + \int_{\mathcal{B}} \mathbf{N}^T \rho \mathbf{N} \ddot{\mathbf{a}}^{t+\Delta t} \, dV = \int_{\mathcal{B}} \mathbf{N}^T \mathbf{b}^{t+\Delta t} \, dV + \int_{\partial\mathcal{B}} \mathbf{N}^T \mathbf{t}^{t+\Delta t} \, dS, \quad (26)$$

and the averaging equation is derived as:

$$\int_{\mathcal{B}} (\mathbf{h} \mathbf{h}^T + c \mathbf{g} \mathbf{g}^T) (\mathbf{e}^t + \Delta \mathbf{e}) \, dV = \int_{\mathcal{B}} \mathbf{h} (\tilde{\boldsymbol{\epsilon}}^t + \Delta \tilde{\boldsymbol{\epsilon}}) \, dV, \quad (27)$$

where  $\mathbf{B} = \mathbf{L} \mathbf{N}$  and  $\mathbf{g}^T = \nabla \mathbf{h}^T$ . Finally, the matrix system of Eq. (22) is derived. The following submatrices and subvectors are defined:

$$\mathbf{K}_{aa} = \int_{\mathcal{B}} \mathbf{B}^T \mathbf{E}_{\tan}^t \mathbf{B} \, dV \quad \text{and} \quad \mathbf{K}_{ae} = - \int_{\mathcal{B}} \mathcal{G}^t \mathbf{B}^T \hat{\boldsymbol{\sigma}}^t \mathbf{h}^T \, dV, \quad (28)$$

$$\mathbf{K}_{ea} = - \int_{\mathcal{B}} \mathbf{h} [\boldsymbol{\xi}^{\text{T}}]^t \mathbf{B} \, dV \quad \text{and} \quad \mathbf{K}_{ee} = \int_{\mathcal{B}} (\mathbf{h} \mathbf{h}^{\text{T}} + c \mathbf{g} \mathbf{g}^{\text{T}}) \, dV, \quad (29)$$

$$\mathbf{f}_{\text{ext}}^{t+\Delta t} = \int_{\mathcal{B}} \mathbf{N}^{\text{T}} \mathbf{b}^{t+\Delta t} \, dV + \int_{\partial \mathcal{B}} \mathbf{N}^{\text{T}} \mathbf{t}^{t+\Delta t} \, dS \quad \text{and} \quad \mathbf{f}_{\text{int}}^t = \int_{\mathcal{B}} \mathbf{B}^{\text{T}} \boldsymbol{\sigma}^t \, dV, \quad (30)$$

$$\mathbf{f}_{\epsilon}^t = \int_{\mathcal{B}} \mathbf{h} \tilde{\epsilon}^t \, dV \quad \text{and} \quad \mathbf{f}_e^t = \mathbf{K}_{ee} \mathbf{e}^t. \quad (31)$$

$\mathbf{E}_{\text{tan}}^t$  is the tangent material stiffness at time  $t$ . Additional definitions are introduced:

$$\mathcal{G}^t = \left[ \frac{d\omega}{d\kappa^d} \right]^t \quad \text{and} \quad \boldsymbol{\xi}^t = \left[ \frac{\partial \tilde{\epsilon}}{\partial \boldsymbol{\epsilon}} \right]^t. \quad (32)$$

In the absence of damage growth  $\mathbf{K}_{ae} = \mathbf{0}$ . Hence, the equations of motion in Eq. (22) are uncoupled from the averaging equation.

## REFERENCES

1. R. Alessi, J.-J. Marigo, S. Vidoli, Gradient damage models coupled with plasticity: Variational formulation and main properties, *Mechanics of Materials*, **80**: 351–367, 2015.
2. H. Askes, J. Pamin, R. de Borst, Dispersion analysis and element-free Galerkin solutions of second- and fourth-order gradient-enhanced damage models, *International Journal for Numerical Methods in Engineering*, **49**: 811–832, 2000.
3. Z.P. Bažant, T. Belytschko, Wave propagation in a strain-softening bar: exact solution, *ASCE Journal of Engineering Mechanics*, **111**(3): 381–389, 1985.
4. Z.P. Bažant, M. Jirásek, Nonlocal integral formulations and damage: Survey of progress, *ASCE Journal of Engineering Mechanics*, **128**(11): 1119–1149, 2002.
5. Z.P. Bažant, G. Pijaudier-Cabot, Nonlocal continuum damage, localization instability and convergence, *ASME Journal of Applied Mechanics*, **55**: 287–293, 1988.
6. T. Belytschko, D. Lasry, A study of localization limiters for strain-softening in statics and dynamics, *Computers & Structures*, **33**(3): 707–715, 1989.
7. N. Bićanić, C.J. Pearce, D.R.J. Owen, Failure predictions of concrete like materials using softening Hoffman plasticity model, [in:] H. Mang, N. Bićanić, R. de Borst [Eds], *Computational modelling of concrete structures, Euro-C 1994*, vol. 1, pp. 185–198, Pineridge Press, Swansea, UK, 1994.
8. J. Bobiński, J. Tejchman, Numerical simulations of localization of deformation in quasi-brittle materials within non-local softening plasticity, *Computers & Concrete*, **1**(4): 1–22, 2004.
9. F.L.L.B. Carneiro, A. Barcellos, Tensile strength of concretes, *RILEM Bulletin*, **13**: 97–123, 1953.

10. A. Carosio, K. Willam, G. Etse, On the consistency of viscoplastic formulations, *International Journal of Solids and Structures*, **37**(48): 7349–7369, 2000.
11. K. Cichocki, *Numerical analysis of concrete structures under blast load*, Monograph 145, Koszalin University of Technology, Koszalin, 2008.
12. K. Cichocki, R. Adamczyk, M. Ruchwa, Material modelling for structures subjected to impulsive loading, *Computer Assisted Mechanics and Engineering Sciences*, **6**(2): 231–244, 1999.
13. C. Comi, Computational modelling of gradient-enhanced damage in quasi-brittle materials, *Mechanics of Cohesive-frictional Materials*, **4**(1): 17–36, 1999.
14. R. de Borst, J. Pamin, M.G.D. Geers, On coupled gradient-dependent plasticity and damage theories with a view to localization analysis, *European Journal of Mechanics A/Solids*, **18**(6): 939–962, 1999.
15. J.H.P. de Vree, W.A.M. Brekelmans, M.A.J. van Gils, Comparison of nonlocal approaches in continuum damage mechanics, *Computers & Structures*, **55**(4): 581–588, 1995.
16. J.-F. Dubé, G. Pijaudier-Cabot, Ch. La Borderie, Rate dependent damage model for concrete in dynamics, *Journal of Engineering Mechanics*, **122**(10): 939–947, 1996.
17. G. Duvaut, I.J. Lions, *Les Inequations en Mécanique et en Physique*, Dunod, Paris, France, 1972.
18. J. Eibl, P.H. Bischoff, G. Lohrmann, Failure mechanics of fibre-reinforced concrete and pre-damaged structures: dynamic loading conditions, Technical Report BRITE/EURAM P-89-3275, Univ. of Karlsruhe, Karlsruhe, Germany, 1994.
19. N. Erarslan, D.J. Williams, Experimental, numerical and analytical studies on tensile strength of rocks, *International Journal of Rock Mechanics and Mining Sciences*, **49**: 21–30, 2012.
20. International Federation for Structural Concrete (fib), *Structural Concrete. The Textbook on Behaviour, Design and Performance. Updated knowledge of the CEB/FIP Model Code 1990*, vol. 1, Bulletin No 1, fib, 1999.
21. M.G.D. Geers, R. de Borst, W.A.M. Brekelmans, R.H.J. Peerlings, Strain-based transient-gradient damage model for failure analyses, *Computer Methods in Applied Mechanics and Engineering*, **160** (1–2): 133–153, 1998.
22. I.M. Gitman, H. Askes, L.J. Sluys, Coupled-volume multi-scale modelling of quasi-brittle material, *European Journal of Mechanics A/Solids*, **27**(3): 302–327, 2008.
23. A. Glema, T. Łodygowski, On importance of imperfections in plastic strain localization problems in materials under impact loading, *Archives of Mechanics*, **54**(5–6): 411–423, 2002.
24. R. Glemberg, *Dynamic analysis of concrete structures*, Ph.D. dissertation, Chalmers University of Technology, Gothenburg, 1984.
25. P. Grassl, M. Jirásek, Plastic model with non-local damage applied to concrete, *International Journal for Numerical and Analytical Methods in Geomechanics*, **30**: 71–90, 2006.
26. U. Häußler-Combe, M. Kitzig, Modeling of concrete behavior under high strain rates with inertially retarded damage, *International Journal of Impact Engineering*, **36**(9): 1106–1115, 2009.

27. O.M. Heeres, A.S.J. Suiker, R. de Borst, A comparison between the Perzyna viscoplastic model and the Consistency viscoplastic model, *European Journal of Mechanics A/Solids*, **21**: 1–12, 2002.
28. D.A. Hordijk, *Local approach to fatigue of concrete*, Ph.D. dissertation, Delft University of Technology, Delft, 1991.
29. L.M. Kachanov, Time of rupture process under creep conditions [in Russian], *Izd. Akad. Nauk SSSR, Otd. Tekh. Nauk*, **8**: 26–31, 1958.
30. L. Kaczmarczyk, C.J. Pearce, N. Bičanić, E. de Souza Neto, Numerical multiscale solution strategy for fracturing heterogeneous materials, *Computer Methods in Applied Mechanics and Engineering*, **199**(17): 1100–1113, 2010.
31. S.-K. Lee, S.-K. Woo, Y.-C. Song, Softening response properties of plain concrete by large-scale direct tension test, *Magazine of Concrete Research*, **60**(1): 33–40, 2008.
32. T. Li, J.-J. Marigo, D. Guilbaud, S. Potapov, Gradient damage modeling of brittle fracture in an explicit dynamics context, *International Journal for Numerical Methods in Engineering*, **108**(11): 1381–1405, 2016.
33. T. Liebe, P. Steinmann, Two strategies towards geometrically non-linear isotropic gradient damage, *Journal of the Mechanical Behaviour of Materials*, **13**: 175–194, 2002.
34. I. Marzec, J. Tejchman, A. Winnicki, Computational simulations of concrete behaviour under dynamic conditions using elasto-visco-plastic model with non-local softening, *Computers & Concrete*, **15**(4): 515–545, 2015.
35. J. Mazars, G. Pijaudier-Cabot, Continuum damage theory – application to concrete, *ASCE Journal of Engineering Mechanics*, **115**: 345–365, 1989.
36. L. Nilsson, *Impact loading on concrete structures. A constitutive modelling, FE analysis, and experimental study of nonlinear wave propagation*, Number 79:1, Chalmers Univ. of Tech., Dept. of Structural Mechanics, Göteborg, Sweden, 1979.
37. J. Ožbolt, J. Bošnjak, E. Sola, Dynamic fracture of concrete compact tension specimen: Experimental and numerical study, *International Journal of Solids and Structures*, **50**: 4270–4278, 2013.
38. J. Pamin, Gradient plasticity and damage models: a short comparison, *Computational Materials Science*, **32**: 472–479, 2005.
39. J. Pamin, A. Wosatko, Static gradient damage simulations using stabilized finite elements, *Journal of Theoretical and Applied Mechanics*, **50**(3): 841–853, 2012.
40. R.R. Pedersen, A. Simone, L.J. Sluys, An analysis of dynamic fracture in concrete with a continuum visco-elastic visco-plastic damage, *Engineering Fracture Mechanics*, **75**(13): 3782–3805, 2008.
41. R.H.J. Peerlings, R. de Borst, W.A.M. Brekelmans, J.H.P. de Vree, Gradient-enhanced damage for quasi-brittle materials, *International Journal for Numerical Methods in Engineering*, **39**(19): 3391–3403, 1996.
42. R.H.J. Peerlings, M.G.D. Geers, R. de Borst, W.A.M. Brekelmans, A critical comparison of nonlocal and gradient-enhanced softening continua, *International Journal of Solids and Structures*, **38**(44–45): 7723–7746, 2001.
43. P. Perzyna, Fundamental problems in viscoplasticity, [in:] *Recent Advances in Applied Mechanics*, vol. 9, pp. 243–377, New York, USA, 1966, Academic Press.

44. C. Rocco, G.V. Guinea, J. Planas, M. Elices, Mechanisms of rupture in splitting tests, *ACI Materials Journal*, **96**: 52–60, 1999.
45. J.G. Rots, *Computational modeling of concrete fracture*, Ph.D. dissertation, Delft University of Technology, Delft, 1988.
46. G. Ruiz, M. Ortiz, A. Pandolfi, Three-dimensional finite-element simulation of the dynamic Brazilian tests on concrete cylinders, *International Journal for Numerical Methods in Engineering*, **48**: 963–994, 2000.
47. J.C.J. Schellekens, *Computational strategies for composite structures*, Ph.D. dissertation, Delft University of Technology, Delft, 1992.
48. J.C. Simo, J.W. Ju, Strain- and stress-based continuum damage models – I. Formulation, II. Computational aspects, *International Journal of Solids and Structures*, **23**(7): 821–869, 1987.
49. A. Simone, H. Askes, R.H.J. Peerlings, L.J. Sluys, Interpolation requirements for implicit gradient-enhanced continuum damage models, *Communications in Numerical Methods in Engineering*, **19**: 563–572, 2003 (see also [50]).
50. A. Simone, H. Askes, R.H.J. Peerlings, L.J. Sluys, Corrigendum 'Interpolation requirements for implicit gradient-enhanced continuum damage models', *Communications in Numerical Methods in Engineering*, **20**: 163–165, 2004.
51. A. Simone, H. Askes, L.J. Sluys, Incorrect initiation and propagation of failure in non-local and gradient-enhanced media, *International Journal of Solids and Structures*, **41**(2): 351–363, 2004.
52. E.C. Simons, J. Weerheijm, L.J. Sluys, A viscosity regularized plasticity model for ceramics, *European Journal of Mechanics A/Solids*, **72**: 310–328, 2018.
53. Ł Skarżyński, M. Nitka, J. Tejchman, Modelling of concrete fracture at aggregate level using FEM and DEM based on X-ray  $\mu$ CT images of internal structure, *Engineering Fracture Mechanics*, **147**: 13–35, 2015.
54. L.J. Sluys, *Wave propagation, localization and dispersion in softening solids*, Ph.D. dissertation, Delft University of Technology, Delft, 1992.
55. L.J. Sluys, Dynamic failure in reinforced concrete structures, [in:] G.M.A. Kusters, M.A.N. Hendriks [Eds], *DIANA Computational Mechanics '94*, pp. 193–203, Kluwer Academic Publishers, Dordrecht, 1994.
56. L.J. Sluys, R. de Borst, Failure in plain and reinforced concrete – an analysis of crack width and crack spacing, *International Journal of Solids and Structures*, **33**: 3257–3276, 1996.
57. A. Stolarski, W. Cichorski, Numerical analysis of a reinforced concrete beam and a deep beam under impulsive loading, *Computer Assisted Mechanics and Engineering Sciences*, **12**(4): 299–328, 2005.
58. R.L. Taylor, FEAP – A Finite Element Analysis Program, Version 7.4, User manual, University of California at Berkeley, Berkeley, 2001.
59. J.W. Tedesco, C.A. Ross, S.T. Kuennen, Experimental and numerical analysis of high strain rate splitting tensile tests, *ACI Materials Journal*, **90**(2): 162–169, 1993.
60. D.-K. Thai, S.-E. Kim, Failure analysis of reinforced concrete walls under impact loading using the finite element approach, *Engineering Failure Analysis*, **45**: 252–277, 2014.

61. J.G.M. van Mier, *Strain-softening of concrete under multiaxial loading conditions*, Ph.D. dissertation, Eindhoven University of Technology, Eindhoven, 1984.
62. R.A. Vonk, *Softening of concrete loaded in compression*, Ph.D. dissertation, Eindhoven University of Technology, Eindhoven, 1992.
63. T. Waffenschmidt, C. Polindara, A. Menzel, B. Sergio, A gradient-enhanced large-deformation continuum damage model for fibre-reinforced materials, *Computer Methods in Applied Mechanics and Engineering*, **268**: 801–842, 2014.
64. W.M. Wang, *Stationary and propagative instabilities in metals – a computational point of view*, Ph.D. dissertation, Delft University of Technology, Delft, 1997.
65. Z. Wang, L.H. Poh, A homogenized localizing gradient damage model with micro inertia effect, *Journal of the Mechanics and Physics of Solids*, **116**: 370–390, 2018.
66. B. Wcisło, J. Pamin, K. Kowalczyk-Gajewska, Gradient-enhanced damage model for large deformations of elastic-plastic materials, *Archives of Mechanics*, **65**(5): 407–428, 2013.
67. A. Winnicki, Crack closing effect in damage mechanics, [in:] W. Biliński [Ed.], *Proc. XII Conf. Computer Methods in Design and Analysis of Hydrostructures*, pp. 155–164, Cracow University of Technology, Cracow, 2000.
68. A. Winnicki, Viscoplastic and internal discontinuity models in analysis of structural concrete, Series Civil Engineering, Monograph 349, Cracow University of Technology, Cracow, 2007.
69. A. Winnicki, C.J. Pearce, N. Bićanić, Viscoplastic Hoffman consistency model for concrete, *Computers & Structures*, **79**: 7–19, 2001.
70. A. Wosatko, A. Genikomsou, J. Pamin, M.A. Polak, A. Winnicki, Examination of two regularized damage-plasticity models for concrete with regard to crack closing, *Engineering Fracture Mechanics*, **194**: 190–211, 2018.
71. A. Wosatko, J. Pamin, A. Winnicki, Gradient damage in simulations of behaviour of RC bars and beams under static and impact loading, *Archives of Civil Engineering*, **52**(1): 455–477, 2006.
72. A. Wosatko, A. Winnicki, J. Pamin, Numerical analysis of Brazilian split test on concrete cylinder, *Computers & Concrete*, **8**(3): 243–278, 2011.

*Received October 31, 2019; revised version January 13, 2020.*